

AIM: Software and Hardware Co-design for Architecture-level IR-drop Mitigation in High-performance PIM

Yuanpeng Zhang

School of Integrated Circuits
Peking University
Beijing, China
Beijing Advanced Innovation Center
for Integrated Circuits
Beijing, China
zyp_cs@pku.edu.cn

Zhihang Yuan

Houmo AI
Nanjing, China
hahnyuan@gmail.com

Zhao Wang

School of Integrated Circuits
Peking University
Beijing, China
School of Computer Science
Peking University
Beijing, China
wangzhao21@pku.edu.cn

Wei Gao

Houmo AI
Shanghai, China
wei.gao@houmo.ai

Xing Hu

Houmo AI
Nanjing, China
xing.hu@houmo.ai

Cong Li

School of Integrated Circuits
Peking University
Beijing, China
Beijing Advanced Innovation Center
for Integrated Circuits
Beijing, China
leesou@pku.edu.cn

Chenguang Zhang

School of Integrated Circuits
Peking University
Beijing, China
School of Computer Science
Peking University
Beijing, China
zhangchg@stu.pku.edu.cn

Qiang Wu

Houmo AI
Nanjing, China
qiang.wu@houmo.ai

Guangyu Sun*

School of Integrated Circuits
Peking University
Beijing, China
Beijing Advanced Innovation Center
for Integrated Circuits
Beijing, China
gsun@pku.edu.cn

Xi Chen

Southeast University
Nanjing, China
xichen@seu.edu.cn

Jingchen Zhu

School of Integrated Circuits
Peking University
Beijing, China
School of Computer Science
Peking University
Beijing, China
zjc990112@pku.edu.cn

Xin Si

Southeast University
Nanjing, China
xinsi@seu.edu.cn

Runsheng Wang

School of Integrated Circuits
Peking University
Beijing, China
Beijing Advanced Innovation Center
for Integrated Circuits
Beijing, China
wrs@pku.edu.cn

Abstract

SRAM Processing-in-Memory (PIM) has emerged as the most promising implementation for high-performance PIM, delivering superior computing density, energy efficiency, and computational precision. However, the pursuit of higher performance necessitates more complex circuit designs and increased operating frequencies, which exacerbate IR-drop issues. Severe IR-drop can significantly degrade chip performance and even threaten reliability. Conventional circuit-level IR-drop mitigation methods, such as back-end optimizations, are resource-intensive and often compromise power, performance, and area (PPA). To address these challenges, we propose AIM, comprehensive software and hardware co-design for architecture-level IR-drop mitigation in high-performance PIM. Initially, leveraging the bit-serial and in-situ dataflow processing properties of PIM, we introduce R_{tog} and HR, which establish a direct correlation between PIM workloads and IR-drop. Building on this foundation, we propose LHR and WDS, enabling extensive exploration of architecture-level IR-drop mitigation while maintaining computational accuracy through software optimization. Subsequently, we develop IR-Booster, a dynamic adjustment mechanism that integrates software-level HR information with hardware-based IR-drop monitoring to adapt the V-f pairs of the PIM macro, achieving enhanced energy efficiency and performance. Finally, we propose the HR-aware task mapping method, bridging software and hardware designs to achieve optimal improvement. Post-layout simulation results on a 7nm 256-TOPS PIM chip demonstrate that AIM achieves up to 69.2% IR-drop mitigation, resulting in 2.29 \times energy efficiency improvement and 1.152 \times speedup.

CCS Concepts

• **Computer systems organization** \rightarrow Architectures; • **Hardware** \rightarrow Power and energy; • **Computing methodologies** \rightarrow Machine learning; • **Security and privacy** \rightarrow Security in hardware.

Keywords

Processing-in-memory, IR-drop mitigation, Architecture-level optimization, Software and hardware co-design

ACM Reference Format:

Yuanpeng Zhang, Xing Hu, Xi Chen, Zhihang Yuan, Cong Li, Jingchen Zhu, Zhao Wang, Chenguang Zhang, Xin Si, Wei Gao, Qiang Wu, Runsheng Wang, and Guangyu Sun. 2025. AIM: Software and Hardware Co-design for Architecture-level IR-drop Mitigation in High-performance PIM. In *Proceedings of the 52nd Annual International Symposium on Computer Architecture (ISCA '25)*, June 21–25, 2025, Tokyo, Japan. ACM, New York, NY, USA, 18 pages. <https://doi.org/10.1145/3695053.3730987>

*Corresponding author

Permission to make digital or hard copies of all or part of this work for personal or classroom use is granted without fee provided that copies are not made or distributed for profit or commercial advantage and that copies bear this notice and the full citation on the first page. Copyrights for components of this work owned by others than the author(s) must be honored. Abstracting with credit is permitted. To copy otherwise, or republish, to post on servers or to redistribute to lists, requires prior specific permission and/or a fee. Request permissions from permissions@acm.org.

ISCA '25, Tokyo, Japan

© 2025 Copyright held by the owner/author(s). Publication rights licensed to ACM.

ACM ISBN 979-8-4007-1261-6/2025/06

<https://doi.org/10.1145/3695053.3730987>

1 Introduction

Processing-in-memory (PIM) circuit seamlessly combines storage and computing functions, embedding computational capabilities within the memory to enhance data processing efficiency [4, 13, 23, 62, 97]. Compared to eNVMs and DRAM, SRAM-based PIM (SRAM PIM) offers higher computational precision and achieves superior energy efficiency and computing density by leveraging state-of-the-art (SOTA) CMOS process technologies [25, 46, 78, 89, 93, 94]. For instance, TSMC's latest SRAM PIM design, utilizing 3nm process technology, achieves 55.0 TOPS/mm^2 and 32.5 TOPS/W while supporting $\text{INT}12 \times \text{INT}12$ computations [25]. Consequently, SRAM PIM has been extensively studied in academia as a computing paradigm with substantial development potential [16, 25, 30, 34, 61, 71, 86, 87, 89–91, 95] and is widely regarded as the leading candidate for commercial high-performance PIM chips. Numerous companies and startups have developed commercial SRAM PIM products for various AI scenarios. Examples include d-matrix [20] for large language model serving, Houmo [36] for autonomous driving, MediaTek [78] and PIMCHIP [69] for mobile devices, as well as Axelera [5], Synthara [83], and Surecore [81] for IoT applications, etc. Among these, d-Matrix's Corsair platform is specifically designed for generative AI applications in data centers, delivering up to 9600-TFLOPS computational power while offering superior power efficiency, reduced latency, and lower total cost of ownership (TCO) [20]. Similarly, Houmo's MoMagic30 [37], an edge AI chip, delivers up to 100-TOPS computing power with a typical power consumption of 12W, supporting mainstream large language models (LLMs) and achieving performance of 15–20 tokens per second. Additionally, MediaTek has integrated TSMC's 3nm SRAM PIM Engine into its smart devices [78]. These advancements underscore the promise of SRAM PIM as a high-performance solution for efficient AI processing.

Nevertheless, during the design and signoff process of a high-performance PIM chip, we found that it faces the challenge of severe **IR-drop**. IR-drop is a phenomenon where the supply voltage is influenced by current within a functioning circuit, resulting in increased clock delay and even reliability failures [6, 12, 65]. This problem is a widespread issue in all types of chips, including AI processors, CPUs, and GPUs [11, 44, 45, 74, 77]. And it is especially pronounced in high-performance PIM chips, where the simultaneous operation of numerous computing logic units within the same cycle generates substantial instantaneous current. Typically, hardware engineers rely on various circuit-level IR-drop mitigation strategies to ensure functionality and safety. These strategies include cell relocations, modifications to power planes, and the addition of decoupling capacitors [8, 9, 42, 53]. However, such methods require significant time and resources, often compromising the chip's performance, power, and area (PPA) [7, 51, 59]. For example, the Graphcore Bow IPU [29] employs wafer-on-wafer (WoW) 3D packaging technology and incorporates deep trench capacitors (DTCs) in the power delivery die near the computing units to mitigate a 100mV IR-drop [28], resulting in great design cost and energy consumption. Similarly, we observed an even higher IR-drop of 140mV in our commercially available 7nm 256-TOPS SRAM PIM chip. These challenges highlight the critical need for architecture-level IR-drop mitigation methods to reduce design costs while improving chip performance and power efficiency.

Architecture-level IR-drop mitigation requires establishing a clear relationship between IR-drop and workload characteristics. Unlike general-purpose computing units, PIM architectures possess unique opportunities in this regard. First, PIM workloads are inherently more regular and often pre-determined. PIM chips are primarily designed for neural network workloads and, in specific scenarios such as autonomous driving [55, 96], even only execute a limited set of specialized models. It simplifies the task of analyzing workload characteristics. Second, PIM naturally supports in-situ processing [93, 94], enabling the decoupling of input and weight data, thereby allowing optimizations without being affected by user input variability. Leveraging these characteristics, we proposed AIM, a comprehensive software and hardware co-design for Architecture-level IR-drop Mitigation on high-performance PIM. To the best of our knowledge, we are the first to mitigate IR-drop in high-performance PIM from an architectural perspective. Our contributions are multifaceted:

- We propose R_{tog} (instantaneous toggle rate of bitstreams in a PIM bank) and HR (average hamming rate of weights), two architecture-level metrics correlating workloads and IR-drop.
- We introduce LHR (lower hamming rate), a regularization term to reduce HR by penalizing high-HR weights with negligible accuracy loss during quantization. The code¹ for integrating LHR with quantization algorithms has been open-sourced.
- We present WDS (weight distribution shift), a software method leveraging data distribution to further reduce HR.
- We develop IR-Booster, a dynamic V-f pairs adjustment method combining software-derived HR information and hardware-based IR-drop monitoring to achieve IR-drop mitigation while improving energy efficiency and performance.
- We introduce HR-aware task mapping, a strategy that incorporates HR when mapping tasks to hardware units controlled by IR-Booster, achieving optimal performance of software and hardware collaboration.

We validate AIM using post-layout simulation data obtained from RedHawk [3] and HSPICE [82] on a 7nm 256-TOPS PIM chip design. Experimental results demonstrate that AIM achieves up to 69.2% IR-drop mitigation, resulting in up to 2.29× energy efficiency improvement or 1.152× performance improvement.

2 Background

2.1 SRAM PIM

SRAM PIM has emerged as a promising architecture for high-performance computing, offering exceptional computing density, energy efficiency, and computational precision. These advantages are rooted in SRAM’s rapid access times ($\sim 1\text{ns}$ read/write latency), high endurance, and utilization of state-of-the-art CMOS process technologies [46, 71, 80, 94]. In SRAM PIM architectures, many multiplicands stored in SRAM cells engage in bit-wise multiplication with input multipliers, with subsequent accumulation performed through dedicated paths. Throughout the entire matrix-matrix multiplication process, the data in SRAM cells remains unchanged, and input data is loaded bit-serially, referred to as **in-situ processing**. This approach substantially reduces energy consumption while

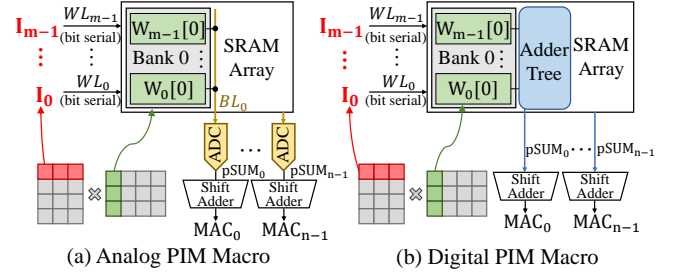


Figure 1: SRAM PIM and data placement

achieving fast multiply-accumulate (MAC) operations. SRAM PIM architectures can be categorized into two types based on their data accumulation format: Analog PIM (APIM) [79] and Digital PIM (DPIM) [78]. As shown in Figure 1-(a), in APIM, the products are accumulated as an analog bit-line (BL) voltage, which is subsequently converted to a digital value by an analog-to-digital converter (ADC). In contrast, DPIM relies entirely on digital representation, where data processing and computation occur via the outputs of logic gates and adder trees (Figure 1-(b)). This digital approach minimizes the effects of Process-Voltage-Temperature (PVT) variations, thereby improving operational reliability [30, 34, 47, 78, 89, 90].

Although APIM and DPIM differ in the form of product accumulation, they share similarities in data placement and processing paradigm. As shown in Figure 1, this paper designates the multiplied data stored in SRAM as **in-memory data** (denoted as W) and the serialized data sequentially loaded on the word line (WL) as **input data** (denoted as I). Specifically, for operations involving fixed weights, such as convolution layers (conv), weights are typically in-memory data, while features are loaded as input data. Conversely, for variable-operand operators such as QK^T or SV in transformer attention, either matrix can act as in-memory data, depending on the specific configuration and shape of the operation.

2.2 A Brief Introduction to IR-drop

IR-drop represents the voltage discrepancy between the ideal supply voltage and the actual voltage received by each circuit cell (Figure 2-(a)). The magnitude of the IR-drop is positively correlated with the product of current (I) passing through the power delivery network (PDN) parasitic resistance (R). IR-drop can be classified into static IR-drop and dynamic IR-drop, distinguished by the origins and behaviors of corresponding currents.

Static IR-drop is caused by static current. Static current is drawn by an integrated circuit when it is idle, unloaded, and not actively switching, but still enabled. It is generally equivalent to the leakage current, denoted as I_{lk} in Figure 2-(b), which represents the gradual flow of electrical charge across boundaries that are typically viewed as insulating, such as current leakage through transistors in the “off” state. Static IR-drop is primarily influenced by the PDN design, as well as the placement and routing of the circuit.

Dynamic IR-drop is caused by dynamic current, which occurs when the integrated circuit is in operation. It mainly consists of two types of current: short-circuit current and switching current. As illustrated in Figure 2-(b), short-circuit current, denoted as I_{sc} , arises when there is an instantaneous short-circuit connection between

¹<https://github.com/pku-zyp/LHR-of-AIM-in-ISCA25.git>

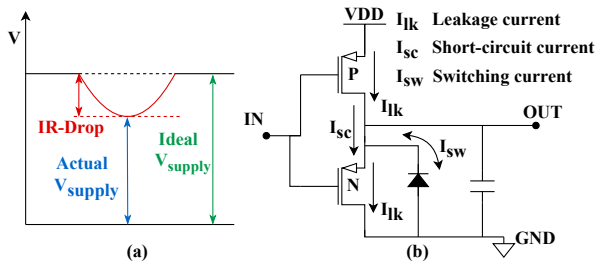


Figure 2: (a) IR-drop (b) Static and dynamic current

the supply voltage and ground during a gate state transition. Switching current, represented as I_{sw} , is produced through the charging and discharging of internal and net capacitances. Dynamic IR-drop is thus highly sensitive to runtime activities, including gate switching and the capacitive charge and discharge cycles.

3 Motivation

3.1 IR-drop Impact and Circuit-level Mitigation

As chip performance advances and frequency increases, the IR-drop problem is becoming more and more serious. For digital chips, including DPIM, CPUs, GPUs, and TPUs [11, 44, 45, 74, 77], significant IR-drop reduces the voltage to standard cells, impairing performance and leading to time violations such as setup/hold violations [6, 12, 65]. Furthermore, a severe IR-drop that prevents a cell from meeting the minimum operational voltage can result in the chip’s functional failure [17]. For analog chips, like APIM, IR-drop directly affects the BL voltage used for calculations, degrading energy efficiency and computational accuracy [27, 48, 49].

To mitigate these effects, IC designers are compelled to adopt numerous time-intensive and costly circuit-level mitigation techniques, often compromising the chip’s performance, power, and area (PPA) metrics [8, 9, 42, 53]. These interventions include widening power supply lines, increasing the density of power switches, adjusting switch placement within floorplan channels and boundaries [18, 35, 51, 66, 85], inserting decoupling capacitors [43], and managing timing slack by optimizing clock tree structures [10]. In spite of these efforts, careful clock frequency planning remains necessary to prevent timing violations induced by IR-drop under extreme conditions. Moreover, we found that although the circuit-level mitigation techniques have a good effect on static IR-drop, it is too pessimistic when mitigating dynamic IR-drop.

3.2 Opportunity and Challenges

To ensure chip reliability and prevent IR-drop violations under any workload, IC designers typically employ rigorous testbenches for chip design and signoff [15, 56, 67, 73]. This includes evaluating the IR-drop under the theoretically most demanding workload, recorded as the signoff worst-case IR-drop. However, circuit-level IR-drop mitigation techniques targeting the worst-case IR-drop are too pessimistic, revealing the opportunity for optimization for two main reasons. First, unlike general-purpose computing cores, high-performance PIM architectures are specifically tailored to support AI applications, making their workloads more predictable and deterministic. By sequentially mapping operators from several

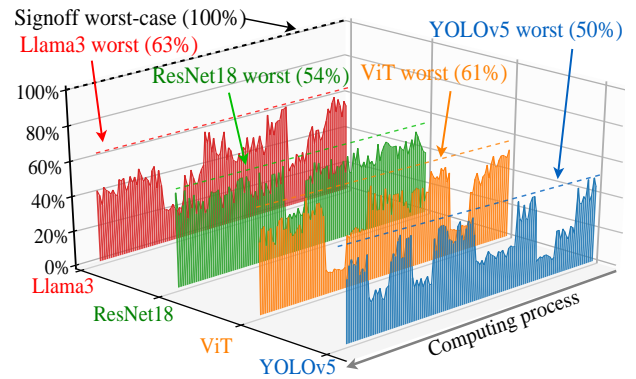


Figure 3: Normalized IR-drop at different workloads

workloads onto a 256-TOPS SRAM PIM and profiling the IR-drop during processing, we observe significant discrepancies compared to the signoff worst-case. As illustrated in Figure 3, while IR-drop fluctuates significantly during processing, the worst IR-drop of different workloads remains considerably lower than the signoff worst-case. Moreover, we find that the worst IR-drop for each model exhibits a relatively stable pattern with different input images or texts. These phenomena indicate a potential correlation between workloads and IR-drop. Second, PIM naturally supports in-situ dataflow processing and bit-serial multiplication, resulting in an observable data behavior model. By identifying and exploiting the relationship between workloads and IR-drop, architecture-level IR-drop mitigation strategies can be developed to avoid the pessimism in circuit-level IR-drop mitigation.

Despite the opportunity, there are still several challenges to be solved. 1) The foundation of architecture-level IR-drop mitigation lies in identifying the correlation between workload and IR-drop and expressing it in a statistically manageable form. Blindly testing all workloads and measuring IR-drop is neither cost-effective nor feasible, given the vast number of models and the large size of datasets. 2) Profiling results show that the model itself accounts for only about 30%-50% of the available architectural IR-drop mitigation space, necessitating low-cost software methods to further expand this space. 3) The available mitigation space varies across models, and even the IR-drop can differ significantly between operators within the same model. This requires software-guided hardware dynamically supporting various IR-drop degrees.

4 Correlating Workload and IR-drop

In this section, we lay the groundwork for AIM. Building on the definition and characteristics of IR-drop, we propose R_{tog} , which represents the instantaneous toggle rate of bitstreams from SRAM cells to the adder component in a PIM bank. This metric serves as an architecture-level indicator that quantitatively captures the correlation between IR-drop and workload. We validate the effectiveness of R_{tog} through experiments. Additionally, we propose HR, defined as the average hamming rate of quantized weights, as a simplified and optimizable metric derived from R_{tog} , which is input data independent. HR enables more effective exploration of architecture-level IR-drop mitigation strategies.

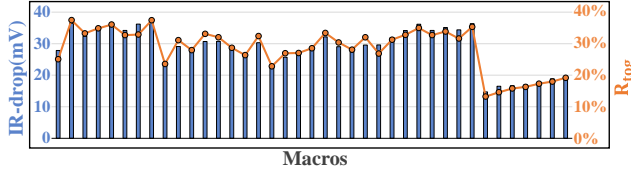


Figure 4: Correlation of IR-drop and R_{tog}

4.1 R_{tog} : an Architecture-level IR-drop Indicator

Many previous works [12, 65, 76, 84] and commercial tools [3, 82] commonly use gate-level bit toggle rates to evaluate circuit IR-drop. These tools model the power network and combine it with toggle rates obtained from logic simulations to simulate current distributions and calculate the IR-drop across components.

Inspired by these circuit-level IR-drop estimation tools, which correlate dynamic current through components with nearby circuit activities, we propose R_{tog} , an architecture-level indicator linking workload characteristics directly to IR-drop. R_{tog} quantifies the cycle-to-cycle toggle rate of bitstreams from SRAM cells to the adder component in a PIM bank. Given in-memory data $\{W_k\}_{k=1}^n$ stored in a PIM bank with n cells. Each W_k is quantized to q bits and the bit values are denoted as $W_{k,1}, \dots, W_{k,q}$. The input data at cycle t and $t+1$ are $\{I_{k,t}\}_{k=1}^n$ and $\{I_{k,t+1}\}_{k=1}^n$. R_{tog} of a PIM bank in cycle t is expressed as the Equation 1:

$$\text{in cycle } t, R_{\text{tog}} = \frac{\sum_{k=1}^n \sum_{i=1}^q (W_{k,i} \wedge (I_{k,t} \oplus I_{k,t+1}))}{nq} \quad (1)$$

The IR-drop can be roughly estimated by Equation 2:

$$\begin{aligned} \text{IR-drop} &= \Delta V_{\text{static}} + \Delta V_{\text{dynamic}} \\ \Delta V_{\text{static}} &\approx k_{lk} I_{lk} R_{lk} \\ \Delta V_{\text{dynamic}} &\approx (k_{sc} I_{sc} R_{sc} + k_{sw} I_{sw} R_{sw}) \times R_{\text{tog}} \end{aligned} \quad (2)$$

where I_{lk} , I_{sc} , and I_{sw} represent leakage, short-circuit, and switching currents, respectively, while R_{lk} , R_{sc} , and R_{sw} are the corresponding resistances. k_{lk} , k_{sc} , and k_{sw} are constant coefficients.

Unlike circuit-level tools that require complex modeling and simulations, R_{tog} simplifies IR-drop estimation by treating the PIM bank as a whole area with relatively stable equivalent resistance. While this approach sacrifices precise per-component estimations, R_{tog} serves as a robust indicator for maintaining a partial order relationship with IR-drop, aligning well with intuition: higher R_{tog} typically reflects increased IR-drop activities.

To validate R_{tog} , we conducted experiments on 7nm DPIM macro and 28nm APIM macros, estimating IR-drop using HSPICE [82]. The average R_{tog} across all banks in a PIM macro correlates strongly with IR-drop, achieving coefficients of 0.977 for DPIM and 0.998 for APIM across various workloads. Figure 4 shows the linear correlation results between IR-drop and R_{tog} of the DPIM macros.

4.2 HR: an Optimizable Metric for Mitigation

Although R_{tog} is an accurate architecture-level indicator, it varies dynamically with workloads, especially input streams. R_{tog} can exceed 10^8 toggles for a single input image. It makes real-time software analysis infeasible due to resource and practicality constraints.

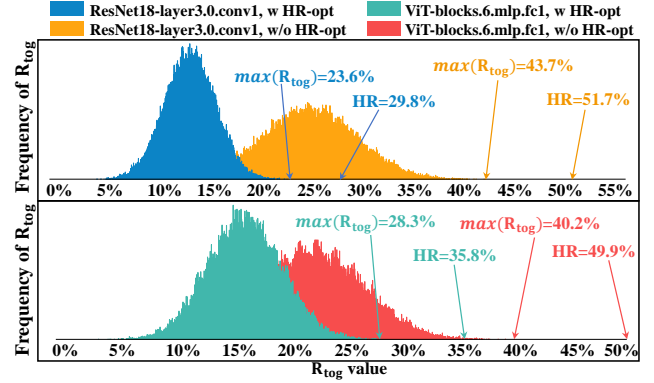


Figure 5: R_{tog} distribution: HR dominates the maximum of R_{tog} and HR optimization reduces overall R_{tog}

To address this, we introduce HR (Hamming Rate), an optimizable metric derived from R_{tog} . The core idea behind HR is to leverage the in-situ processing and bit-serial properties of PIM architectures, decoupling the pre-loaded data (network weights) from the dynamic input feature streams. HR is defined as Equation 3.

$$\begin{aligned} HM(\{W_n\}) &:= \sum_{i=1}^q \sum_{k=1}^n W_{k,i} \\ HR(\{W_n\}) &:= \frac{HM(\{W_n\})}{nq} \end{aligned} \quad (3)$$

Where $HM(\{W_n\})$ represents the hamming value of $\{W_n\}$, counting all valid bits (1s) in $\{W_k\}$. HR is the hamming value divided by nq , determined only by in-memory data (W).

$$\therefore \forall k, \forall t, s_{k,t} \oplus s_{k,t+1} = \{0, 1\} \leq 1$$

$$\therefore R_{\text{tog}} = \frac{\sum_{k=1}^n \sum_{i=1}^q (W_{k,i} \& (I_{k,t} \oplus I_{k,t+1}))}{nq} \leq \frac{\sum_{k=1}^n \sum_{i=1}^q W_{k,i}}{nq} \quad (4)$$

$$\therefore \text{sup}(R_{\text{tog}}) = \frac{\sum_{k=1}^n \sum_{i=1}^q W_{k,i}}{nq} = HR(\{W_n\})$$

Equation 4 establishes that HR represents the theoretical upper bound of R_{tog} when all input bitstreams toggle concurrently. Experiment results further support this. As shown in Figure 5, we profiled the R_{tog} distribution of a ResNet18/ViT operator over 50,000 cycles (consistent trends hold across other layers and networks). Notably, the observed peak R_{tog} never exceeds the corresponding HR value, with a substantial margin between the two. Moreover, optimizing HR helps reduce the overall value of R_{tog} .

Therefore, by optimizing the pre-loaded in-memory data, HR allows us to mitigate IR-drop without accounting for input stream variations, offering a practical, architecture-level solution.

5 AIM Design

5.1 AIM Overview

As illustrated in Figure 6, AIM is structured into two complementary components: offline software-based HR optimization and a runtime hardware adjustment method guided by software. These

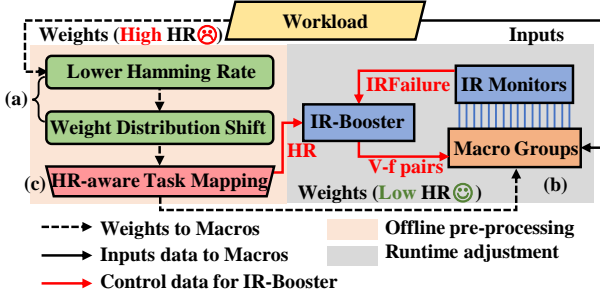


Figure 6: AIM design and workflow: (a) Offline software-based HR optimization methods: LHR and WDS (b) A runtime adjustment hardware method: IR-Booster (c) An interconnection and co-optimization method: HR-aware task mapping

components are interconnected through HR-aware task mapping to enable cohesive system-level optimization. In Section 5.2, we first outlined the basic implementation and usage of each component, and provided an end-to-end example to demonstrate their synergy. We then detailed the design principles and methodologies of each component. Specifically, in Section 5.3, we introduce LHR, a lightweight regularization term integrated into the quantization process. This term reduces the HR of weights during pre-processing, improving robustness without significantly impacting accuracy. In Section 5.4, building on post-quantization data distribution and its HR characteristics, we propose WDS, a method that refines the overall distribution to further reduce the weighted HR of the network. In Section 5.5, we present IR-Booster, a runtime hardware-level adjustment mechanism that combines software-derived HR information with hardware-based IR-drop monitoring. By dynamically selecting optimal voltage-frequency pairs for each PIM macro, IR-Booster mitigates IR-drop at the architectural level while enhancing energy efficiency and performance. Finally, in Section 5.6, we propose HR-aware task mapping, which assigns segmented tasks to PIM macros managed by IR-Booster. It maximizes IR-Booster’s effectiveness, further optimizing overall system performance.

5.2 Application Integration and Usage

5.2.1 AIM component: implementation and selection.

Each method of AIM is implemented independently, offering flexibility for selective use based on user needs.

(1) LHR: It integrates easily into the application layer by adding a term to training loop (e.g., $\text{loss} += \lambda * \text{lhr_norm}(\text{model.parameters}())$, in PyTorch). It requires no modifications to underlying frameworks (such as PyTorch, TensorFlow, or JAX) due to its gradient-based design, requiring only standard API calls without low-level hacking.

(2) WDS: Integrated within the compiler, WDS has a default δ value of 8. However, users can explicitly specify different δ values for each operator supported by the compiler.

(3) IR-Booster: Directly integrated into the PIM chip as a hardware technique, IR-Booster operates independently of LHR when fine-tuning is not feasible (e.g., due to privacy concerns). IR-Booster alone can provide significant energy efficiency improvements, with LHR and WDS providing even greater benefits.

(4) HR-aware Task Mapping: Integrated within the compiler, it is applied after determining the operator scheduling and segmentation. Its primary goal is to reduce performance degradation caused by mutual interference when networks with different HR values are mapped onto the PIM chip simultaneously. Since it involves multiple rounds of simulation introducing second-level latency, this method should be used cautiously. For complex workloads (especially those with various operators or networks), we recommend utilizing HR-aware Task Mapping for optimal IR-drop mitigation.

5.2.2 Synergy of all AIM components: an end-to-end example.

All the software methods and hardware technologies in AIM work in concert to deliver optimal improvements. We present an end-to-end example of how they collaborate.

During the processing phase, AIM begins by loading the target network weights, which have been optimized using the quantized architecture enhanced with LHR. The compiler then reads the δ configuration for each operator and performs WDS operations to adjust weights accordingly. Next, the compiler applies a simulated annealing-based task mapping strategy, using the HR values obtained during processing and input data randomly drawn from standard datasets (e.g., ImageNet [72], Wikitext2 [60]). These HR values corresponding to all mapped tasks are passed to IR-Booster.

Once the compilation is complete and the optimized weights are loaded, AIM enters the inference phase. During runtime, IR-Booster dynamically selects V-f pairs based on the user’s selected operating mode. It also continuously monitors for IRFailures and triggers recalculation when necessary. This integrated approach allows AIM to achieve substantial energy efficiency and processing performance improvements while maintaining reliability.

5.3 Lower Hamming Rate

In this section, we introduce LHR (lower hamming rate), a regularization to decrease the HR throughout the entire network with minimum accuracy influence during quantization. By targeting the layers with the highest HR, LHR aims to mitigate IR-drop at the network level. Unlike many energy-aware quantization methods, LHR prioritizes reducing the HR of critical layers over only achieving a theoretically minimal overall average HR.

Regularization terms are commonly added to loss functions during Quantization Aware Training (QAT) to enforce additional constraints. A straightforward approach to reducing HR would involve applying the L_1 norm to penalize weights with higher HR. However, HR is a non-differentiable integer metric, making it unsuitable for backpropagation. To overcome this, we approximate the HR of a floating-point weight w using a linear interpolation between its two nearest integer values. This allows us to define a differentiable approximation of HR, enabling its use in backpropagation.

$$\begin{aligned} \text{low} &= \lfloor \frac{w}{s_w} \rfloor, \quad \text{high} = \lceil \frac{w}{s_w} \rceil, \quad p = \frac{w}{s_w} - \text{low} \\ \text{HR}(w) &= (1 - p) \cdot \text{HR}[\text{low}] + p \cdot \text{HR}[\text{high}] \end{aligned} \quad (5)$$

Given a floating-point weight w and its quantization scale s_w , we determine the nearest integers low and high . Using $\text{HR}[\]$ to represent the HR value of the corresponding integer, we calculate interpolated HR of floating-point weight w as Equation 5.

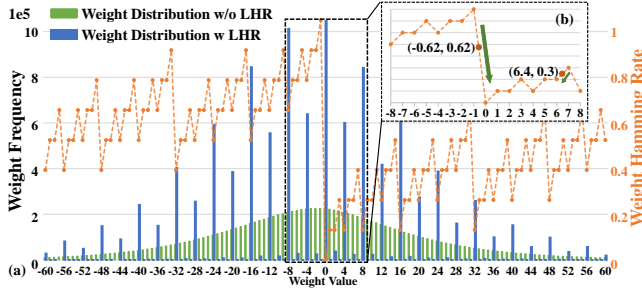


Figure 7: (a) Weight distribution with LHR aligns with local minima of the Hamming Rate (b) Calculating the HR and corresponding gradient of a floating-point by interpolation

During backpropagation, the gradient of w is derived from the slope of the interpolated line segment. This gradient encourages weights to converge toward regions with lower HR. For example, in Figure 7-(b), the interpolated HR of -0.62 is 0.62 , with a gradient of 1 , while the HR of 6.4 is 0.3 , with a gradient of -0.125 . Larger differences in HR between adjacent integers lead to steeper gradients, enabling faster convergence to optimal values.

LHR can be incorporated into either quantization fine-tuning or directly into quantization algorithms. For a classification task, the total loss function with LHR is expressed as:

$$L_{HR} = \sum_{i=1}^n HM_{rate}^2(layer_i) \quad (6)$$

$$L_{all} = L_{Task} + \lambda L_{HR}$$

Where L_{Task} represents the original task-specific loss (e.g., cross-entropy for classification), and λ is a regularization parameter used to balance the HR reduction and accuracy loss. L_{HR} represents the hamming loss of the network, calculated by the squared sum of the average HR for each layer in the entire network. This penalizes layers with higher HR, thereby reducing both the overall network's HR and especially the peak HR across all layers.

To validate LHR, we profile the quantized weight distribution of ResNet18. As shown in Figure 7-(a), compared to the widely adopted quantization method [64] as a baseline without HR considering, the introduction of LHR encourages weights to align with local minima of the Hamming function, such as -8 , 0 , and 8 . This alignment reduces HR of weights, effectively mitigating IR-drop.

5.4 Weight Distribution Shift

While LHR reduces the overall HR by encouraging weights to converge at local minima of HR, quantization generally preserves the relative sign (positive or negative) of weights [1, 24, 63, 75]. This means weights remain normally distributed, with more weights concentrated near zero and small magnitudes (e.g., -8 and 8), as shown in Figure 7. According to the rules of two's complement encoding, positive values with smaller absolute magnitudes have lower HR, whereas negative values with smaller absolute magnitudes exhibit higher HR. This observation motivates us to propose weight distribution shift (WDS), which reduces overall HR by shifting the data distribution towards positive values, concentrating weights around smaller positive numbers.

Algorithm 1 Weight distribution shift

```

1: for Layer in {Layers} do
2:   /* Offline preprocessing (Outside Critical Path): */
3:   for Weight in Layer do
4:     Weight' = IfOverflow(INTMAXnbit, (Weight +  $\delta$ ))
5:   end for
6:   /* MM multiplication with lower HR (On Critical Path): */
7:   Output = Matmul(Layer', Input)
8:   /* Shift compensation (Outside Critical Path): */
9:   Correc = -Sum(Input)  $\times$   $\delta$ , Output = Output + Correc
10: end for
    
```

5.4.1 Weight Distribution Shift Methodology.

Shifting the weight distribution towards positive values can be implemented by adding a constant value, δ , to all weights offline. This adjustment occurs immediately after quantization. Although this shift reduces the HR of weights used for matrix multiplications, it introduces numerical errors that can significantly degrade the accuracy of the neural network. Therefore, it is essential to compensate for these errors after the matrix multiplication operation. Algorithm 1 illustrates the process of WDS.

1) Offline preprocessing: To minimize IR-drop during matrix-matrix multiplication (line 7), δ is added to weights offline before they are loaded (lines 3-5). If the resulting weight value exceeds the maximum representable value for the quantization bitwidth (e.g., INT8), it is clamped to $INTMAX$. This avoids overflow into negative values, which could otherwise cause unknown errors and degrade inference accuracy. Profiling reveals such overflows occur in less than 1% of weights, minimizing their impact. When selecting δ values, we notice that weights processed through quantization with LHR often cluster at local minima with lower hamming, such as 0 , -8 , or 8 (Figure 7-(a)). Therefore, δ must be chosen to align with this pattern; improper selection could inadvertently increase HR. For INT8 quantization, δ values of 8 or 16 produce better results. While for INT4 quantization, δ values of 2 or 4 are more suitable.

2) Shift compensation: Errors introduced by δ are corrected post-matrix multiplication. First, the *Correction* value is calculated by *Input* and δ (line 9). Since all weights in a layer share the same δ , the *Input* values are summed before being multiplied by δ to simplify hardware and reduce multiplications. Subsequently, in line 10, the *Correction* is added to the *Output* to rectify the calculation errors. Detailed hardware support for shift compensation is as follows.

5.4.2 Shift Compensator Hardware Design.

Alleviating the computational error caused by WDS while ensuring the correction step stays off the critical path is central to the design of the shift compensator (SC). Figure 8 presents its design, which is strategically located next to PIM macro Banks, sharing input streams to optimize resource usage. The SC performs three main operations: ① Correction calculation: This step involves summing the inputs, multiplying the sum by δ , and inverting the result. Since δ is a power of 2, multiplication simplifies to a bit-shifting operation, significantly reducing computational cost. ② Correction term broadcast: All banks within a Macro share the same input streams and δ values, allowing a single correction term to be broadcast

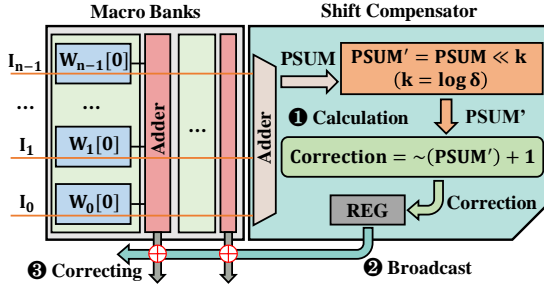


Figure 8: Shift compensator design: supporting correction term calculation, broadcast and correcting

across all banks. This shared design minimizes hardware redundancy and simplifies the design. ③ Pipelined correcting: To ensure the correction process does not interfere with the critical path, a register is inserted after the correction term calculation. This allows the MAC operation to proceed concurrently with the correction term computation. In the next cycle, the correction term is applied to the MAC output via a pipelined binary addition.

5.5 IR-Booster Design

While LHR and WDS effectively reduce the HR of neural network weights using quantization algorithms and data distribution techniques, achieving comprehensive architecture-level IR-drop mitigation requires a synergistic software-guided hardware approach. Two primary challenges necessitate this integration. 1) Dynamic mitigation requirements: The available architecture-level mitigation space varies significantly across different neural networks and even operators within the same network. The effectiveness of LHR and WDS also differs across workloads. The hardware must dynamically adapt to provide optimal mitigation levels. 2) Input-determined operators: For operators where in-memory data and input data both depend on runtime processing (e.g., QK^T and SV in attention), weight-based optimizations such as LHR and WDS are insufficient. It highlights real-time IR-drop monitoring and dynamic hardware control for IR-drop mitigation.

To address these challenges, we propose IR-Booster. Leveraging hardware-based dynamic adjustments and a safety monitoring mechanism, IR-Booster allows macros to operate at lower voltages and higher frequencies, thus enhancing energy efficiency and chip performance. Specifically, IR-Booster first reserves voltage-frequency pairs for different R_{tog} gradients, ensuring safe operation across corresponding IR-drop intensities for Macro Groups during hardware design signoff. Then, during compilation, IR-Booster gathers the weight HR information for each Macro after task mapping is completed. Since HR represents the upper bound of R_{tog} , the safe voltage and frequency for each task are determined during pre-processing. At runtime, IR-Booster can aggressively adjust the voltage and frequency, while maintaining chip reliability through a hardware-based IRFailure detection and recalculation mechanism.

5.5.1 IR-Booster V-f Pair Adjustment.

As illustrated in Figure 10-(a), due to hardware design requirements, multiple PIM macros are integrated into a **Macro Group**, sharing a unified power supply and operating at the same frequency.

Table 1: Safe level and corresponding initialized a-level (%)

safe level	100	60	55	50	45	40	35	30	25	20
a-level ₀	60	40	35	35	35	30	30	25	20	20

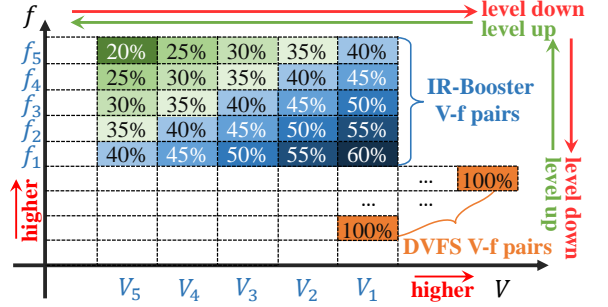


Figure 9: IR-Booster and DVFS V-f pairs: level up of V-f pairs means lower voltage or higher frequency or both of them

For each Macro Group, IR-Booster provides a selection of voltage-frequency pairs, referred to as **V-f pairs**, each associated with a specific R_{tog} value. These V-f pairs define operational conditions under which the macro Group can safely function without exceeding the designated R_{tog} . Hardware engineers validate these pairs when the Macro Group is issued as an independent IP (intellectual property), ensuring reliability for the specified R_{tog} levels.

IR-Booster can be regarded as an extension of Dynamic Voltage and Frequency Scaling (DVFS) technology. Figure 9 illustrates the main differences between IR-Booster pairs and traditional DVFS technology (noting that the figure depicts trends rather than linear relationships in value): DVFS ensures the chip reliability by still signing off V-f pairs with the worst-case IR-drop conditions (that is $R_{\text{tog}}=100\%$) [2, 31, 32, 40]. Therefore, DVFS could only increase/decrease voltage and frequency simultaneously based on the urgency of the processor's current tasks. In contrast, IR-Booster leverages the architecture-level IR-drop margin to enable more flexible and granular adjustments. That is, IR-Booster can reduce voltage while maintaining the operating frequency or increase frequency while holding the power supply conditions constant.

A series of V-f pairs corresponding to the same R_{tog} value form a subset, and their corresponding R_{tog} value is recorded as **level**. Based on workload profiling, we first define the V-f pair level range to be 20%~60%. Sensitivity analysis indicates that narrowing this range by 5% results in over 17% loss in IR-drop mitigation capability, while widening the range has minimal improvement (<3%). Additionally, using a step of 6% (4x4 V-f pairs) or larger leads to more than 8% loss in capability, as fewer V-f pairs affect fine-grained control. While a step below 5% can yield better IR-drop mitigation (~6%), increasing the number of V-f pairs to 36 or more significantly raises hardware design complexity and cost, which is unacceptable. Therefore, the V-f pair level step is set to 5%.

For a given operator, IR-Booster first selects a **safe level** that can ensure reliable operation based on HR optimization results from LHR and WDS. Then, IR-Booster determines a more performance-

Algorithm 2 IR-Booster level adjustment for each Macro Group

```

1: initialize:  $SafeCounter = 0$ ,  $a-Level = a-Level_0$ 
2:  $Level = a-Level$  /*(Start with a-Level)*/
3: for Each Cycle do
4:   if  $IRFailure == True$  then
5:      $Level = SafeLevel$  /*(Set Safe Level)*/
6:     if  $SafeCounter < 0.2\beta$  then
7:       set:  $SafeCounter = 0$ 
8:        $a-Level = Down(a-Level)$  /*(a-Level Down)*/
9:     end if
10:    set:  $SafeCounter = 0$ 
11:   else if Macro frequency adjustment in same Set then
12:      $Level = Set-Level$  /*(Frequency Synchronization)*/
13:     set:  $SafeCounter = 0$ 
14:   else
15:      $SafeCounter ++$ 
16:     if  $SafeCounter == \beta$  then
17:        $Level = a-Level$  /*(Back to a-Level)*/
18:     end if
19:     if  $SafeCounter > 2\beta$  then
20:        $a-Level = UP(a-Level)$  /*(a-Level Up)*/
21:        $Level = a-Level$ 
22:       set:  $SafeCounter = \beta$ 
23:     end if
24:   end if
25: end for

```

or energy-efficient **aggressive level** according to the safe level and adjusts it based on the feedback from the hardware IR Monitor.

Software-guided safe level selection: For operators like conv, Q/K/V generation, and linear layers, where their weights are the in-memory data, the HR of each macro and the worst HR in each Group (HR_G) can be pre-determined after task mapping. Using HR_G , IR-Booster selects the nearest higher R_{tog} level (rounded to the nearest 5%) as the safe level. For example, if HR_G is 47.5%, the safe level is set to 50%, and the optional V-f pairs are $\{V_3-f_1, V_4-f_2, V_5-f_3\}$. The safe level of Groups with $HR_G > 60\%$ revert to DVFS (100% R_{tog}), which is quite rare after LHR and WDS optimization. For input-determined operators such as QK^T and SV in transformer attention, both in-memory data and input data are generated from preceding calculations. Their HR values cannot be offline pre-determined by the algorithm, and thus, these operators default to a 100% safe level.

IRFailure-aware aggressive level adjustment: After selecting a safe level, IR-Booster aims to operate at an aggressive level (a-level) that provides higher performance or energy efficiency. This process uses real-time feedback from the IR Monitor to iteratively refine the a-level, as outlined in Algorithm 2. IRFailure-aware aggressive level adjustment mainly consists of three parts: 1) Initialization: IR-Booster initializes with an $a-level_0$ derived from the pre-determined safe level (lines 1-2). The values for $a-level_0$, shown in Table 1, are determined based on profiling results. This aligns with the intuition that a higher safe level provides greater remaining utilization space for optimization. 2) IRFailure-driven level adjustment: Whenever IR-drop violation occurs, the level is set to the safe level to ensure the chip reliability (lines 4-5). If the failure interval is too short (less than 0.2β), it indicates that the a-level is overly aggressive, prompting

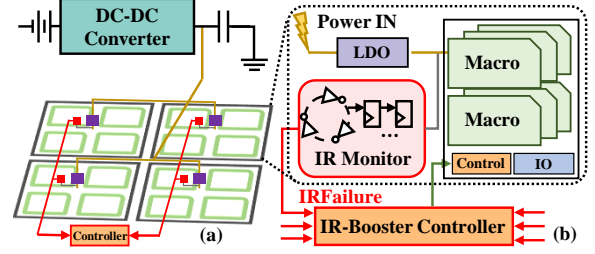


Figure 10: (a) Power supply and V-f adjustment at Macro Group granularity (b) IR-Booster regulated by IRFailure

IR-Booster to level down (lines 6-9). 3) A-level optimization: If the Macro Group operates without failures for continuous β cycles, the a-level is restored (lines 13-14). If safe operation extends beyond 2β cycles, the a-level is increased by 5% (level up), unlocking additional performance or power savings (lines 16-19).

Sprint mode and low-power mode: After determining the R_{tog} level, IR-Booster selects an appropriate V-f pair within the subset of this level. IR-Booster offers two modes of operation. In sprint mode, IR-Booster prioritizes high-voltage, high-frequency combinations to maximize throughput. Conversely, when external operating conditions impose constraints (e.g., limitations on heat generation or power consumption rates), IR-Booster operates in low-power mode, favoring low-voltage, low-frequency pairs.

These two modes are designed to simplify user configuration and ensure clearer experimental results. However, the design of IR-Booster fully supports flexible selection of V-f pairs. When using AIM, users can further customize the IR-Booster strategy through the available interfaces to tailor it for specific needs.

5.5.2 IRFailure-driven recomputing mechanism.

To ensure the chip's reliability, detecting IRFailures and performing recomputing after such errors are crucial.

IR Monitor: Building on the design proposed in [21], we introduce a simplified voltage monitoring device called the IR monitor. Each IR monitor comprises multiple inverter (INV) gates configured as a free-oscillating loop, functioning as a Voltage-Controlled Oscillator (VCO). The IR-drop reduces the supply voltage, which in turn affects the VCO's oscillation frequency, enabling a voltage-to-frequency conversion. By sampling and analyzing the VCO's phase, the device generates a corresponding digital signal. If the supply voltage drops below a predefined threshold, the monitor triggers an "IRFailure" signal. As shown in Figure 10-(b), IR monitors are strategically embedded between Macro Groups and their corresponding Low Dropout Regulators (LDOs) to monitor the voltage supplied to all Groups. The "IRFailure" signals from these monitors are sent to the Booster Controller, which oversees the adjustment of voltage-frequency (V-f) pairs and manages recomputing.

Booster Controller: The Booster Controller processes IRFailure signals from all Groups, directing the affected Groups to suspend computation, adjust their V-f pairs, and initiate recomputing. As shown in the Figure 11-(b), task allocation is performed at the macro granularity. During inference, multiple macros from different groups are combined to compute an operator, forming a logical Macro Set. Consequently, while macros within the same physical

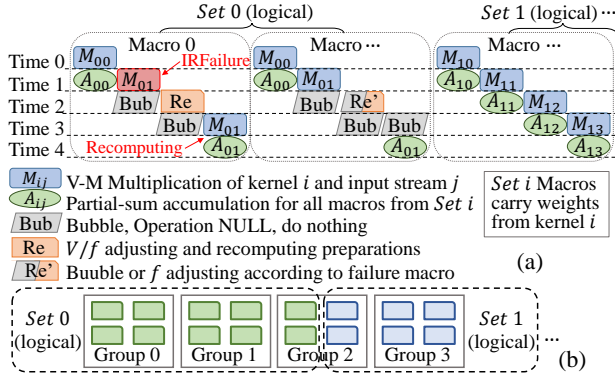


Figure 11: (a) IR-Booster recomputing: minimizing the delay due to interference between macros (b) Macro Set definition

Group share identical frequency and voltage settings, all macros within a logical Set must operate at the same frequency to ensure consistency, even if their voltages could differ. When any macro requires recomputing due to an IRFailure, other macros within the same Set temporarily stall the pipeline and store partial sums until the recomputing completes, ensuring data consistency. Importantly, this process does not disrupt macros in other Sets. For example, as depicted in Figure 11-(a), when an IRFailure is detected in macro 0 of Set 0, the Booster Controller halts the operations of all macros in Set 0. It then instructs macro 0 to adjust its voltage and frequency settings before performing the necessary recomputing. Priority is given to increasing the voltage to maintain the current frequency whenever possible. Other macros in Set 0 do not perform additional computations, thereby minimizing power consumption.

5.6 HR-aware Task Mapping

Increasingly complex application scenarios and models often require multiple operators to run concurrently, significantly complicating task mapping. For instance, UniAD [41], BEVFormer [92], and TransFuse [98]—which combine conv and transformer layers with highly varying HR values—are widely employed in visual perception, autonomous driving, and medical image segmentation, respectively. Even within a single transformer-based model, the HR and corresponding safe levels vary significantly across layers, such as Q/K/V generation, QK^T , SV, and linear layers.

Previous operator scheduling and mapping methods [38, 68, 99] generally assign split operators to the available computing power of a region sequentially after considering operator scheduling and mapping. This approach works well in traditional PIM architectures, where macros operate under uniform conditions with the same fixed V-f pair. However, in PIM chips supported by IR-Booster, once a weight is assigned, each macro has its own independent HR and, consequently, a distinct safe V-f level. Since the PIM chip adjusts the power supply and V-f at the Macro Group level, the macros within a group are constrained by the macro requiring the lowest V-f level. Additionally, macros handling tasks from the same operator must operate at the same frequency. These constraints make it inefficient to assign split operators to PIM macros using sequential or random mapping strategies, resulting in suboptimal

Algorithm 3 HR-aware Task Mapping Algorithm

```

1: initialize:  $M_{best} \leftarrow M_0, T \leftarrow T_0$ 
2:  $S_{best} \leftarrow S_0 \leftarrow \text{Score}(M_0)$ 
3: for  $i \leftarrow 0$  to Steps do
4:    $T \leftarrow qT, M_{new} = \text{Switch}(M), S_{new} = \text{Score}(M_{new})$ 
5:    $\Delta S = S_{new} - S$ 
6:   if  $\Delta S < 0$  or  $\text{Random}() < \exp(\frac{-\Delta S}{0.5S_0T})$  then
7:     if  $S_{new} < S_{best}$  then
8:        $M_{best} \leftarrow M_{new}, S_{best} \leftarrow S_{new}$ 
9:     end if
10:     $M \leftarrow M_{new}, S \leftarrow S_{new}$ 
11:  end if
12:  if  $\text{End-Condition}()$  then
13:    break
14:  end if
15: end for
16: return  $M_{best}$ 

```

performance. To address this, we propose HR-aware task mapping, which is integrated into the compiler to optimize task-to-macro mapping after operator scheduling and before inference begins.

Exploring all possible task mapping combinations for a PIM chip with 64 macros during compilation is computationally infeasible. Additionally, an absolutely optimal mapping does not exist because of unknown input features. Therefore, we implement Algorithm 3 based on simulated annealing [88]. Key parameters include a temperature reduction coefficient q of 0.95, an initial normalized temperature T_0 of 1, and an iteration limit of 500. We adopt the normalized exponential (NE) acceptor function to minimize the influence of system-level parameter adjustments. It terminates early if ten consecutive attempts are rejected.

The mapping transition function randomly selects two macros and their corresponding tasks from different Groups and exchanges them. Importantly, an “empty macro” option is introduced, allowing one or two macros to remain unmapped in extreme cases. This prevents interference between tasks from different operators with significantly different HR values. The mapping evaluation function relies on a lightweight simulator. Based on profiling input data, the simulator generates a 100-step input flip sequence sampled from a normal distribution, which is then combined with the HR values assigned to each macro. The simulator uses this data to estimate the end-to-end delay and power consumption for the given mapping. If a macro remains vacant in the final mapping plan, it indicates that significant HR disparities prevented tasks from being mapped together, effectively avoiding interference. In such cases, tasks already assigned to the Group can be redistributed evenly across all macros within the Group. It balances the load and reduces the Group’s safe level, further optimizing performance.

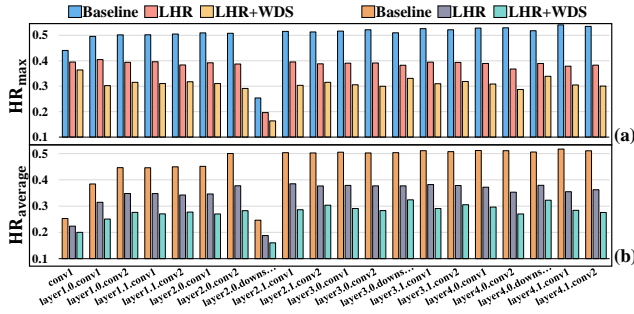
6 Evaluation

6.1 Evaluation Setup

We evaluate the effectiveness of AIM using a combination of software experiment results and hardware post-layout simulation [3]. Specifically, the HR results (Sections 6.2~6.5) are derived from our profiling of the adjusted network weights, while the IR-drop and

Table 2: HR_{average} and HR_{max} reduction over baseline[64]

Model	ResNet18	MobileNet	YOLOv5	ViT	Llama3	GPT2	
HR _{aver}	+LHR	28%	29%	23%	25.9%	25.9%	30.7%
	+WDS($\delta=8$)	39%	30.6%	31.5%	31.9%	30.7%	38%
	+WDS($\delta=16$)	45.6%	33.6%	38.6%	35.6%	36.3%	41.5%
HR _{max}	+LHR	28.6%	30.5%	24.3%	26.8%	26.5%	31.2%
	+WDS($\delta=8$)	37.5%	32.2%	30.7%	32.2%	32%	37.5%
	+WDS($\delta=16$)	44.5%	35.1%	37.6%	36.2%	38.3%	41.2%


Figure 12: HR reduction of each layer in ResNet18 [33]

PPA data (Sections 6.6~6.10) are obtained from the post-layout simulations, a widely trusted method in hardware design. We selected ResNet18 [33], MobileNetV2 [39], and YOLOv5 [14] as conv-based networks, and Llama3.2-1B [22], ViT [19], and GPT2 [70] as transformer-based networks. YOLOv5 uses COCO [54], Llama3.2 and GPT2 utilize Wikitext2 [60], and the remaining networks rely on ImageNet (ILSVRC 2012) [72]. The hardware architecture is a chip design featuring two RISC-V cores and 16 macro groups. Each group contains four macros. The architecture parameters are abstracted from a standard half-height, half-length PCIe acceleration card based on SRAM PIM with support for 16-channel FHD encoding, and a maximum computing power of 256 TOPS.

6.2 HR Decrease and Accuracy Impact

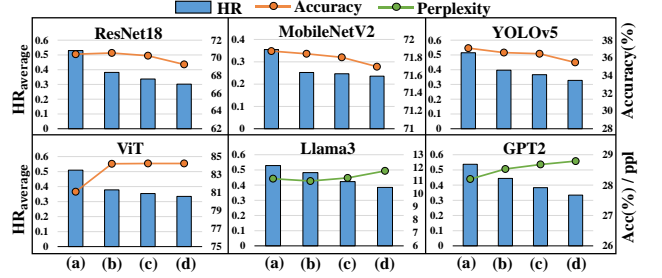
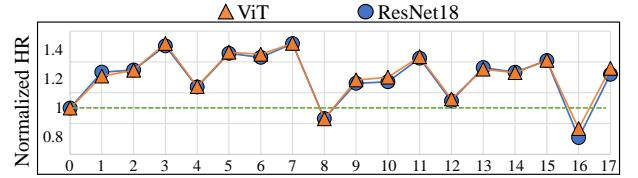
Table 2 demonstrates that both LHR and WDS significantly reduce HR_{max} and HR_{average} compared to the baseline [64], a widely adopted quantization-aware-training (QAT) algorithm. “+LHR” means adding the LHR regularization term on the basis of baseline, and “+WDS(δ)” means adding WDS on the basis of “+LHR”.

Figure 12 provides additional insights by illustrating how LHR and WDS ($\delta = 16$) impact HR across all layers of ResNet18. While initial layers with smaller kernels show imbalanced HR due to under-utilized macros, most layers exhibit similar HR values. This suggests a uniform HR distribution within individual layers and structural homogeneity across similar layers in the network. These findings strongly support our HR-aware task mapping design.

Figure 13 highlights the trade-off between HR reduction and accuracy across different workloads. Applying LHR and WDS yields substantial HR reductions with minimal accuracy degradation. ViT and Llama3 even show improved accuracy. This is because moderate quantization does not notably affect accuracy but enhances the network’s generalization ability. Similar findings have been observed in previous quantization works, such as [57, 58].

Table 3: HR_{average} and accuracy impact on PTQs with LHR

PTQ	OmniQuant [75]				BRECQ [52]			
Model	GPT2		Llama3.2-1B		ResNet18		MobileNetV2	
Metric	HR _{aver}	ppl	HR _{aver}	ppl	HR _{aver}	acc (%)	HR _{aver}	acc (%)
w/o LHR	0.51	28.69	0.53	11.16	0.5	73.02	0.49	69.715
w LHR	0.47	28.72	0.49	10.947	0.47	72.9	0.46	69.71


Figure 13: HR Decreasing and Accuracy Influence for: (a) Baseline [64] (b) +LHR (c) +WDS ($\delta = 8$) (d) +WDS ($\delta = 16$)

Figure 14: Impact of different δ on WDS

6.3 LHR Combination with PTQ Methods

We evaluated the integration post-training-quantization (PTQ) methods with LHR in Table 3, specifically OmniQuant [75] for LLMs and BRECQ [52] for traditional convolutional networks. Since PTQ methods prioritize rapid, resource-constrained quantization and do not involve adjustments or joint training of the original model, their ability to fine-tune weights is limited. As a result, the HR reduction achieved by combining LHR with PTQ methods is slightly less pronounced compared to QAT [64]. Nevertheless, incorporating LHR into PTQ still significantly reduces HR with minimal accuracy loss. This seamless integration demonstrates LHR’s ability to enhance HR performance when combined with various PTQ methods.

6.4 Configuration of δ for WDS

Figure 14 illustrates the impact of the δ selection in the WDS technique on the overall HR of the network, with data normalized to the HR of weights quantized using LHR. Across different workloads, the trend of HR reduction with varying δ values remains consistent, demonstrating the broad applicability of WDS. Aligning with our analysis in Section 5.4, a precise configuration of δ is crucial for achieving HR reduction: for 8-bit quantized weights, only δ values of 8 or 16 effectively reduce HR. Other configurations result in weight distributions that align with higher HR regions, leading to negative effects. This specific choice of δ is governed by the binary 2’s complement representation method. The fact that δ must be



Figure 15: Comparison and combination of LHR&WDS and pruning on ResNet18 and ViT with different sparse target

a power of 2 is the basis for using the shift method in the shift compensator to simplify multiplication calculations.

6.5 Comparison and Combination with Pruning

Figure 15 illustrates the comparison and relationship between our methods and pruning. For the comparison, we employ the open-source SparseML framework alongside the Gradual Magnitude Pruning* [50] to generate networks with varying sparsity levels.

Network pruning can reduce HR, making it a natural candidate for integration with IR-Booster to mitigate IR-drop. However, we introduce LHR and WDS for two key advantages. First, LHR serves as a regularization term during quantization, ensuring that weight values are not drastically altered, which helps maximize inference accuracy. Second, LHR and WDS are orthogonal to pruning, allowing them to be seamlessly combined. When integrated, they can further reduce HR at the cost of a slight accuracy degradation.

Utilizing post-layout simulation [3], we evaluate AIM’s performance based on our 7nm 256-TOPS PIM design. Figure 17-(a) shows the reduction in demand drive current across clock cycles, while Figures 17-(b) and (c) illustrate AIM’s influence on bump current and voltage. “bump” refers to small metal protrusions utilized to establish connections between the chip and its external interfaces, which are essential for reliable chip packaging and interconnection. These metrics are critical for chip design. Notably, AIM achieves reductions in both demanded drive current and bump current, along with a stabilization of bump voltage. This outcome reflects effective IR-drop mitigation and indicates enhanced chip performance.

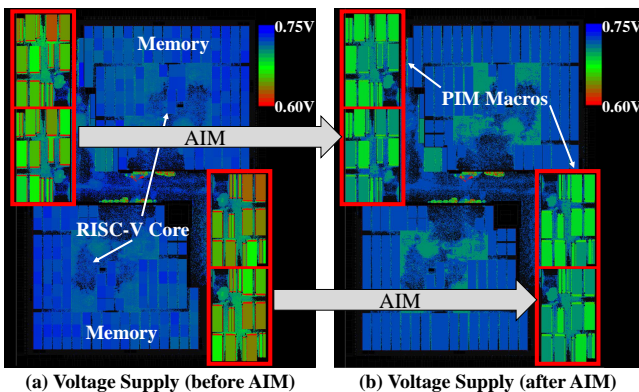


Figure 16: IR-drop mitigation in a 7nm 256-TOPS PIM layout

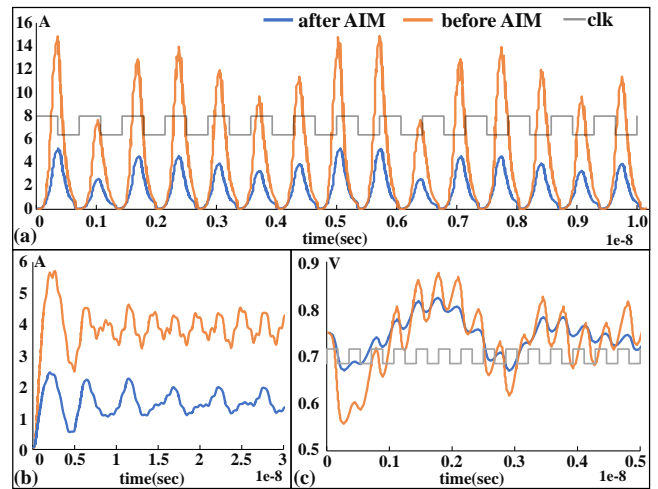


Figure 17: (a) Demanded drive current, (b) Bump voltage, and (c) Bump current before/after AIM

Furthermore, the decrease in current directly reduces power consumption and heat generation, significantly improving the chip’s energy efficiency and thermal management.

6.6 Hardware Results on 256-TOPS PIM Design

Figure 16 illustrates the distribution of IR-drop across the chip layout and the mitigation effects achieved by AIM on the PIM chip. The IR-drop in the RISC-V core and on-chip memory is relatively minimal, with hotspots predominantly concentrated in the PIM macros. This observation is consistent with our earlier analysis, which identified the macros as the primary contributors to significant IR-drop. While AIM’s data adjustments and hardware modifications introduce slight variations in the IR-drop of RISC-V core and memories, these impacts are negligible given the consistency of primary IR-drop hotspots in macros.

According to the post-layout simulation results of the 7nm PIM chip with an operating voltage of 0.75V, AIM can reduce the IR-drop from 140mV to 58.1~43.2mV within a macro, providing 58.5%~69.2% architecture-level IR-drop mitigation. Additionally, AIM provides a 1.91~2.29× improvement in energy efficiency for each macro (4.2978mW→2.243~1.876mW) and enhances overall chip performance by 1.129~1.152× (256TOPS→289~295TOPS) in low-power mode or sprint mode, respectively.

6.7 Trade-off in IR-Booster and β Configuration

Figure 18 shows the impact of various β configurations on IR-Booster performance. Both IR-drop mitigation ability and delay cycles are normalized against IR-Booster operating without aggressive level adjustment (i.e., running exclusively at a safe level). A smaller β value corresponds to tighter clock adjustments, which enhances IR-drop mitigation but increases the occurrence of IRFailures. These failures, in turn, lead to additional delay cycles required to complete the workload. As analyzed in Section 6.8, transformer-based ViT benefits more significantly from IR-Booster’s aggressive adjustments compared to convolution-based workloads. This

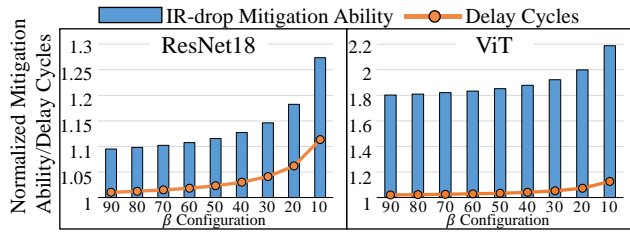


Figure 18: Impact of different β : normalized against IR-Booster operating without aggressive V-f adjustment

difference stems from ViT’s heavier reliance on dynamic, input-dependent operations, which are better supported by IR-Booster’s ability to adaptively mitigate IR-drop.

6.8 Ablation Study

We conducted an ablation experiment to analyze the contribution of each component of AIM. It is important to note that using software operations (LHR, WDS) alone does not directly reduce power consumption or improve performance. Therefore, the data represented by LHR and WDS corresponds to the results obtained with basic IR-Booster support, using a safe-level configuration, to reflect the impact of the software methods. We selected two representative workloads: ViT for transformer-based networks and ResNet18 for convolution-based networks. Although the effects of AIM vary across different workloads, they follow similar trends. Figure 19-(a) demonstrates the IR-drop mitigation effects, while Figure 19-(b) and (c) illustrate the improvements in energy efficiency and processing performance under low-power and sprint modes, respectively.

To isolate the effect of PIM macros from the RISC-V core and other memory components, we evaluate energy efficiency by measuring the average power consumption (in mW) of each macro. Additionally, to assess potential degradation in effective computing power due to IRFailures—i.e., scenarios in which a macro’s failure disrupts the operation of others—we use overall processing performance (in TOPS) as the key metric. This methodology offers a comprehensive understanding of how AIM improves both energy efficiency and computational performance, ensuring that IR-drop mitigation does not compromise system reliability or throughput.

As illustrated in Figure 19, under transformer-based workloads, the primary improvements stem from IR-Booster, whereas for convolution-based workloads, LHR provides the main benefits. This divergence arises from the inherent characteristics of the workloads: For transformer-based workloads, Q, K, and V matrices are all related to user input, preventing effective pre-profiling by software and thus requiring hardware-based IR-drop mitigation. In contrast, conv operators enable pre-optimization and profiling of weights, so software-guided methods can effectively mitigate IR-drop.

Figure 19-(c) also reveals a limitation of IR-Booster in enhancing the chip’s effective performance. Its aggressive voltage adjustment strategy can sometimes lead to IRFailures, requiring recalculations. This decreases the chip’s effective computational power, particularly for workloads involving conv operations. Therefore, aggressive level adjustment and β selection involve a trade-off. For tasks that require faster response, such as real-time inference, enabling

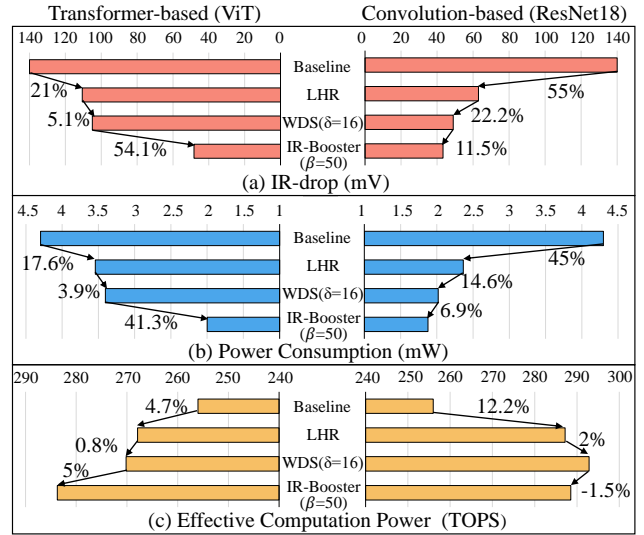


Figure 19: Ablation study in IR-drop, power, and performance

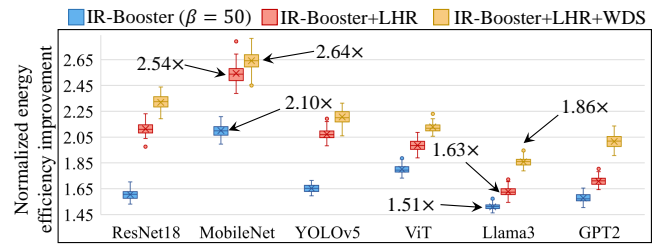


Figure 20: Energy efficiency enhancing of IR-Booster and the improvement of HR optimization method (LHR and WDS)

aggressive adjustment is not recommended. For edge computing devices requiring better energy efficiency, β can be set as needed.

As shown in Figure 20, IR-Booster alone provides significant energy efficiency improvements (1.51–2.10 \times), with LHR and WDS providing even greater benefits.

6.9 HR-aware Task Mapping Validation

Traditional task mapping algorithms consider macros within a PIM chip to be equivalent and therefore rely on naive mapping methods, such as sequential mapping and zigzag mapping [26].

Figure 21 compares the effects of HR-aware task mapping and traditional mapping across different operator combinations. The results indicate that mapping methods that do not explicitly account for HR result in suboptimal performance and energy efficiency under corresponding operating modes. In terms of energy efficiency, poor mapping schemes often group tasks with significantly different HR levels together, which increases power consumption and reduces energy efficiency. In terms of performance, when tasks from different operators are assigned to the same group, a failure in any one task can suspend all tasks within that group. This suspension propagates delays to other tasks of the same operator, severely degrading the overall computational performance.

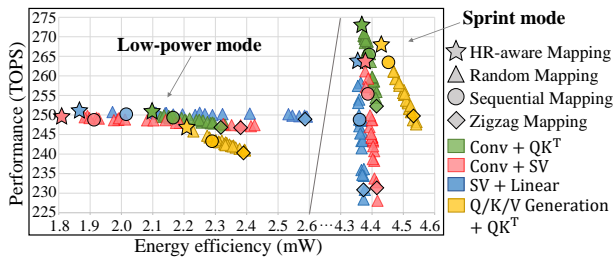


Figure 21: HR-aware task mapping v.s. others

In contrast, HR-aware task mapping explicitly incorporates HR into the mapping process, fully leveraging the IR-drop mitigation benefits of WDS, LHR, and IR-Booster. This approach delivers significant improvements in both performance and power efficiency, underscoring its critical role in maximizing hardware potential.

6.10 Overhead Analysis

6.10.1 Performance overhead.

We have taken a series of measures to avoid the additional delay introduced by the AIM method, such as introducing pipelines in the Shift Compensator to overlap delays and fine-grained macro pause control to reduce mutual interference. However, some overheads are inevitable since V-f adjustments are not instantaneous, and recalculations also introduce extra delay. As shown in Figure 19, an overly aggressive IR-Booster strategy may lead to little performance loss for certain workloads compared to a conservative strategy. However, despite these unavoidable overheads, the various AIM components still result in significant IR-drop mitigation, along with improvements in energy efficiency and overall performance.

6.10.2 Area and power overhead.

To ensure that the shift compensator (SC) does not impact macro throughput, we implement a pipelined design. This approach leverages the PIM macro’s inherent structure, allowing all banks (typically 32, 64, or even 128) within a macro to share a single compensator for lightweight correction computations. Thanks to its simple and efficient design, the compensator introduces minimal overhead, contributing less than 0.2% to the overall chip area and less than 1% to the power consumption of the PIM chip.

IR-Booster adds overhead for IRFailure detection and V-f pair control. Fortunately, due to lower resolution requirements, the simplified IR Monitor design, based on [21], incurs less than 0.1% area overhead and less than 0.5% additional power consumption according to synthesis results from [82]. Moreover, the existing RISC-V core within the PIM chip—originally designed for macro control and general-purpose computations—can be extended to support V-f pair control operations. It ensures that the area and power overhead associated with control remains virtually negligible.

7 Discussion and Future Work

We evaluate the impact of applying AIM to a 28nm 128×32 SRAM APIM macro using [3]. Figure 22-(a) illustrates that AIM achieved approximately 50% IR-drop mitigation on the APIM macro. This result is lower than the 58.5%–69.2% achieved on DPIM. We attribute this disparity to the lower sensitivity of analog circuits to

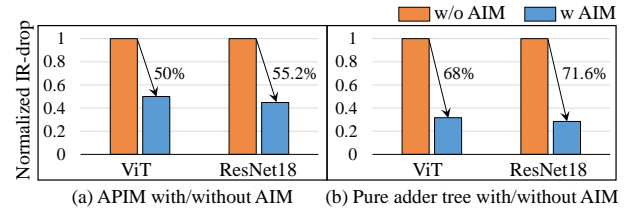


Figure 22: AIM effects on APIM and pure adder tree

IR-drop mitigation. Additionally, we separately model and evaluate the bit-serial adder trees in the DPIM macro, which, as shown in Figure 22-(b), demonstrated notable IR-drop mitigation. These results highlight the potential of AIM for mitigating IR-drop in PIM as well as other AI processors, such as TPUs and GPUs, which rely on complex digital multiplication and accumulation circuits.

AIM can be extended to adapt to PIM designs that support floating-point data types [30, 34], due to their bit-serial and in-situ calculation properties. While the design introduces mantissa alignment and exponent calculations, the core operations—MACs of mantissa—still rely on complement code integer multiplication, making the LHR-like weight fine-tuning and WDS methods applicable. However, the relationship between R_{tog} and IR-drop, as well as how these improvements affect the specific reduction in IR-drop, remains to be explored, and we leave this for future work.

For TPUs and GPUs, a significant challenge arises from their non-bit-serial and non-in-situ MAC implementations, which complicates workload analysis and the correlation with IR-drop. Overcoming these challenges is a promising direction for future research.

8 Conclusion

In this work, we propose AIM from an architecture perspective to address the critical challenge of IR-drop in high-performance PIM, a growing threat to performance and reliability as circuit complexity and operating frequencies increase. By employing software and hardware co-design, AIM effectively mitigates IR-drop while preserving computational accuracy, enhancing energy efficiency, and improving processing performance. It introduces architecture-level IR-drop metrics to quantify and analyze IR-drop characteristics, which form the foundation for proposed software optimizations aimed at IR-drop mitigation. Through the proposed LHR and WDS methods, we effectively mitigate IR-drop via software optimization while computational accuracy is preserved. These software optimizations are further combined with hardware-based dynamic V-f pair adjustments for real-time adaptation by an HR-aware task mapping strategy to maximize overall improvement. Post-layout simulations on a 7nm 256-TOPS PIM design validate that AIM achieves up to 69.2% IR-drop mitigation, delivering a 2.29× improvement in energy efficiency and a 1.152× speedup, providing an efficient solution for IR-drop mitigation in high-performance PIM.

Acknowledgments

We appreciate the valuable feedback and constructive comments from all reviewers and our shepherd. This work is sponsored by National Natural Science Foundation of China (Grant No. 62032001), Beijing Natural Science Foundation L243001, and 111 Project (B18001).

References

- [1] 2023. *Quantizing Large Language Models on Your Laptop (Intel(R) Neural Compressor)*. <https://medium.com/intel-analytics-software/high-performance-low-bit-layer-wise-weight-only-quantization-on-a-laptop-712580899396>
- [2] 2024. *Intel Core™ Processor Family*. <https://www.intel.com/content/www/us/en/products/details/processors/core.html>
- [3] 2024. *RedHawk-SEM*. <https://www.apache-da.com/products/redhawk/redhawk-sem>
- [4] Junghan Ahn, Sungpack Hong, Sungjoo Yoo, Onur Mutlu, and Kiyoungh Choi. 2015. A scalable processing-in-memory accelerator for parallel graph processing. In *2015 ACM/IEEE 42nd Annual International Symposium on Computer Architecture (ISCA)*, 105–117. doi:10.1145/2749469.2750386
- [5] Axelera. 2022. *Metis AI processing units*. <https://www.axelera.ai/blog/digital-in-memory-computing-for-deep-learning-acceleration>
- [6] Yongchan Ban, Changseok Choi, Hosoon Shin, Jaewook Lee, Yongseok Kang, and Woohyun Paik. 2014. Analysis of dynamic voltage drop with PVT variation in FinFET designs. In *2014 International SoC Design Conference (ISOC)*, 132–133. doi:10.1109/ISOC.2014.7087608
- [7] Yongchan Ban, Chenchen Wang, Jia Zeng, and Jongwook Kye. 2017. IR-drop analysis for validating power grids and standard cell architectures in sub-10nm node designs. In *Design-Process-Technology Co-optimization for Manufacturability XI*, Luigi Capodiceci and Jason P. Cain (Eds.), Vol. 10148. International Society for Optics and Photonics, SPIE, 1014810. doi:10.1117/12.2258340
- [8] Sayed Aresh Beheshti-Shirazi, Ashkan Vakil, Sai Manoj, Ioannis Savidis, Houman Homayoun, and Avesta Sasan. 2021. A Reinforced Learning Solution for Clock Skew Engineering to Reduce Peak Current and IR Drop. In *Proceedings of the 2021 on Great Lakes Symposium on VLSI (Virtual Event, USA) (GLSVLSI '21)*. Association for Computing Machinery, New York, NY, USA, 181–187. doi:10.1145/3453688.3461754
- [9] Lakshmi Bhamidipati, Bhoopal Gunna, Houman Homayoun, and Avesta Sasan. 2017. A Power Delivery Network and Cell Placement Aware IR-Drop Mitigation Technique: Harvesting Unused Timing Slacks to Schedule Useful Skews. In *2017 IEEE Computer Society Annual Symposium on VLSI (ISVLSI)*, 272–277. doi:10.1109/ISVLSI.2017.55
- [10] Lakshmi Bhamidipati, Bhoopal Gunna, Houman Homayoun, and Avesta Sasan. 2017. A Power Delivery Network and Cell Placement Aware IR-Drop Mitigation Technique: Harvesting Unused Timing Slacks to Schedule Useful Skews. In *2017 IEEE Computer Society Annual Symposium on VLSI (ISVLSI)*, 272–277. doi:10.1109/ISVLSI.2017.55
- [11] Zhuomin Chai, Yuxiang Zhao, Wei Liu, Yibo Lin, Runsheng Wang, and Ru Huang. 2023. CircuitNet: An Open-Source Dataset for Machine Learning in VLSI CAD Applications With Improved Domain-Specific Evaluation Metric and Learning Strategies. *IEEE Transactions on Computer-Aided Design of Integrated Circuits and Systems* 42, 12 (2023), 5034–5047. doi:10.1109/TCAD.2023.3287970
- [12] H.H. Chen and D.D. Ling. 1997. Power Supply Noise Analysis Methodology For Deep-submicron Vlsi Chip Design. In *Proceedings of the 34th Design Automation Conference*, 638–643. doi:10.1109/DAC.1997.597223
- [13] Yiran Chen, Yuan Xie, Linghao Song, Fan Chen, and Tianqi Tang. 2020. A Survey of Accelerator Architectures for Deep Neural Networks. *Engineering* 6, 3 (2020), 264–274. doi:10.1016/j.eng.2020.01.007
- [14] Raphaël Couturier, Hassan N. Noura, Ola Salman, and Abderrahmane Sider. 2021. A Deep Learning Object Detection Method for an Efficient Clusters Initialization. arXiv:2104.13634 [cs.CV]
- [15] Megha Deogharia, K Madhu Kiran, and Rohit Dhiman. 2024. Drop Analysis for Power Integrity in 3D ICs. In *2024 International Conference on Integrated Circuits, Communication, and Computing Systems (ICIC3S)*, Vol. 1. IEEE, 1–5.
- [16] Giuseppe Desoli, Nitin Chawla, Thomas Boesch, Manui Avodhyawasi, Harsh Rawat, Hitesh Chawla, VS Abhijith, Paolo Zambotti, Akhilesh Sharma, Carmine Cappetta, Michele Rossi, Antonio De Vita, and Francesca Girardi. 2023. 16.7 A 40-310TOPS/W SRAM-Based All-Digital Up to 4b In-Memory Computing Multi-Tiled NN Accelerator in FD-SOI 18nm for Deep-Learning Edge Applications. In *2023 IEEE International Solid-State Circuits Conference (ISSCC)*, 260–262. doi:10.1109/ISSCC42615.2023.10067422
- [17] Sukanta Dey, Satyabrata Dash, Sukumar Nandi, and Gaurav Trivedi. 2018. PGIREM: Reliability-Constrained IR Drop Minimization and Electromigration Assessment of VLSI Power Grid Networks Using Cooperative Coevolution. In *2018 IEEE Computer Society Annual Symposium on VLSI (ISVLSI)*, 40–45. doi:10.1109/ISVLSI.2018.00018
- [18] Sukanta Dey, Satyabrata Dash, Sukumar Nandi, and Gaurav Trivedi. 2018. PGIREM: Reliability-Constrained IR Drop Minimization and Electromigration Assessment of VLSI Power Grid Networks Using Cooperative Coevolution. In *2018 IEEE Computer Society Annual Symposium on VLSI (ISVLSI)*, 40–45. doi:10.1109/ISVLSI.2018.00018
- [19] Alexey Dosovitskiy, Lucas Beyer, Alexander Kolesnikov, Dirk Weissenborn, Xiuhua Zhai, Thomas Unterthiner, Mostafa Dehghani, Matthias Minderer, Georg Heigold, Sylvain Gelly, et al. 2020. An image is worth 16x16 words: Transformers for image recognition at scale. *arXiv preprint arXiv:2010.11929* (2020).
- [20] d-Matrix. 2024. *Corsair*. <https://www.d-matrix.ai/product/>
- [21] Yuxuan Du, Junyi Qian, Zhuo Chen, and Weiwei Shan. 2023. An All-Digital, 1.92–7.32 mV/LSB, 0.5–2 GS/s Sample Rate, and 0-Latency Prediction Voltage Sensor With Dynamic PVT Calibration for Droop Detection and AVS System. *IEEE Transactions on Circuits and Systems I: Regular Papers* 70, 12 (2023), 4888–4899. doi:10.1109/TCSI.2023.3305038
- [22] Abhimanyu Dubey, Abhinav Jauhri, Abhinav Pandey, Abhishek Kadian, Ahmad Al-Dahle, Aiesha Letman, Akhil Mathur, Alan Schelten, Amy Yang, Angela Fan, Anirudh Goyal, Anthony Hartshorn, Aobo Yang, Archi Mitra, Archie Sravankumar, Artem Korenev, Arthur Hinsvark, Arun Rao, Aston Zhang, Aurelien Rodriguez, Austen Gregerson, Ava Spataro, Baptiste Roziere, Bethany Biron, Binh Tang, Bobbie Chern, Charlotte Caucheteux, Chaya Nayak, Chloé Bi, Chris Marra, Chris McConnell, Christian Keller, Christophe Touret, Chunyang Wu, Corinne Wong, Cristian Canton Ferrer, Cyrus Nikolaidis, Damien Allonsius, Daniel Song, Danielle Pintz, Danny Livshits, David Esobu, Dhruv Choudhary, Dhruv Mahajan, Diego Garcia-Olano, Diego Perino, Dieuwke Hupkes, Egor Lakomkin, Ehab Al-Badawy, Elna Lobanova, Emily Dinan, Eric Michael Smith, Filip Radenovic, Frank Zhang, Gabriel Synnaeve, Gabrielle Lee, Georgia Lewis Anderson, Graeme Nail, Gregoire Mialon, Guan Pang, Guillem Cucurell, Hailey Nguyen, Hannah Korevaar, Hu Xu, Hugo Touvron, Iliyan Zarov, Imanol Arrieta Ibarra, Isabel Kloumann, Ishan Misra, Ivan Evtimov, Jade Copet, Jaewon Lee, Jan Geffert, Jana Vranes, Jason Park, Jay Mahadeokar, Jeet Shah, Jelmer van der Linde, Jennifer Billock, Jenny Hong, Jenya Lee, Jeremy Fu, Jianfeng Chi, Jianyu Huang, Jiawen Liu, Jie Wang, Jiecao Yu, Joanna Bitton, Joe Spisak, Jungsoo Park, Joseph Rocca, Joshua Johnstun, Joshua Saxe, Junteng Jia, Kalyan Vasuden Alwala, Kartikeya Upasani, Kate Plawiak, Ke Li, Kenneth Heafield, Kevin Stone, Khalid El-Arini, Krithika Iyer, Kshitiz Malik, Kuenley Chiu, Kunal Bhalla, Lauren Rantala-Yeary, Laurens van der Maaten, Lawrence Chen, Liang Tan, Liz Jenkins, Louis Martin, Lovish Madaan, Lubo Malo, Lukas Blecher, Lukas Landzaat, Luke de Oliveira, Madeline Muzzi, Mahesh Pasupuleti, Mannat Singh, Manohar Paluri, Marcin Kardas, Mathew Oldham, Mathieu Rita, Maya Pavlova, Melanie Kambadur, Mike Lewis, Min Si, Mitesh Kumar Singh, Mona Hassan, Naman Goyal, Narjes Torabi, Nikolay Bashlykov, Nikolay Bogoychev, Niladri Chatterji, Olivier Duchenne, Onur Çelebi, Patrick Alrassy, Pengchuan Zhang, Pengwei Li, Petar Vasic, Peter Weng, Prajjwal Bhargava, Pratik Dubal, Praveen Krishna, Punit Singh Koura, Puxin Xu, Qing He, Qingxiao Dong, Ragavan Srinivasan, Raj Ganapathy, Ramon Calderer, Ricardo Silveira Cabral, Robert Stojnic, Roberta Raileanu, Rohit Girdhar, Rohit Patel, Romain Sauvestre, Ronnie Polidoro, Roshan Sumbaly, Ross Taylor, Ruan Silva, Rui Hou, Rui Wang, Saghar Hosseini, Sahana Chennabasappa, Sanjay Singh, Sean Bell, Seohyun Sonia Kim, Sergey Edunov, Shaoliang Nie, Sharan Narang, Sharath Rapparthi, Sheng Shen, Shengye Wan, Shruti Bhosale, Shun Zhang, Simon Vandenhende, Soumya Batra, Spencer Whitman, Sten Sootla, Stéphane Collet, Suchin Gururangan, Sydney Borodinsky, Tamar Herman, Tara Fowler, Tarek Sheasha, Thomas Georgiou, Thomas Scialom, Tobias Speckbacher, Todor Mihaylov, Tong Xiao, Ujjwal Karn, Vedanuj Goswami, Vibhor Gupta, Vignesh Ramanathan, Viktor Kerkez, Vincent Gonguet, Virginie Do, Vish Vogeti, Vladan Petrovic, Weiwei Chu, Wenhan Xiong, Wenyan Fu, Whitney Meers, Xavier Martinet, Xiaodong Wang, Xiaoqing Ellen Tan, Xinfeng Xie, Xuchao Jia, Xuewei Wang, Yaelle Goldschlag, Yashesh Gaur, Yasmine Babaei, Yi Wen, Yiwen Song, Yuchen Zhang, Yue Li, Yuning Mao, Zacharie Delpierre Coudert, Zheng Yan, Zhengxing Chen, Zoe Papakipos, Aaditya Singh, Aaron Gottafiori, Abha Jain, Adam Kelsey, Adam Shajnfeld, Adithya Gangidi, Adolfo Victoria, Ahuva Goldstand, Ajay Menon, Ajay Sharma, Alex Boesenberg, Alex Vaughan, Alexei Baevski, Allie Feinstein, Amanda Kallet, Amit Sangani, Anam Yunus, Andrei Lupu, Andres Alvarado, Andrew Caples, Andrew Gu, Andrew Ho, Andrew Poulton, Andrew Ryan, Ankit Ramchandani, Annie Franco, Aparajita Saraf, Arkabandhu Chowdhury, Ashley Gabriel, Ashwin Bharambe, Assaf Eisenman, Azadeh Yazdan, Beau James, Ben Maurer, Benjamin Leonhardi, Bernie Huang, Beth Loyd, Beto De Paola, Bhargavi Paranjape, Bing Liu, Bo Wu, Boyu Ni, Braden Hancock, Bram Wasti, Brandon Spence, Brani Stojkovic, Brian Gamido, Britt Montalvo, Carl Parker, Carly Burton, Catalina Mejia, Changhan Wang, Changkyu Kim, Chao Zhou, Chester Hu, Ching-Hsiang Chu, Chris Cai, Chris Tindal, Christoph Feichtenhofer, Damon Civin, Dana Beaty, Daniel Kreymer, Daniel Li, Danny Wyatt, David Adkins, David Xu, Davide Testuggine, Delia David, Devi Parikh, Diana Liskovich, Didem Foss, Dingkang Wang, Duc Le, Dustin Holland, Edward Dowling, Eissa Jamil, Elaine Montgomery, Eleonora Presani, Emily Hahn, Emily Wood, Erik Brinkman, Esteban Arcaute, Evan Dunbar, Evan Smothers, Fei Sun, Felix Kreuk, Feng Tian, Firat Ozgenel, Francesco Caggioni, Francisco Guzmán, Frank Kanayet, Frank Seide, Gabriela Medina Florez, Gabriella Schwarz, Gada Badeer, Georgia Swee, Gil Halpern, Govind Thattai, Grant Herman, Grigory Sizov, Guangyi, Zhang, Guna Lakshminarayanan, Hamid Shojanazeri, Han Zou, Hannah Wang, Hanwen Zha, Haroun Habeeb, Harrison Rudolph, Helen Suk, Henry Aspögren, Hunter Goldman, Ibrahim Damlaj, Igor Molybog, Igor Tufanov, Irina-Elena Veliche, Itai Gat, Jake Weissman, James Geboski, James Kohli, Japhet Asher, Jean-Baptiste Gaya, Jeff Marcus, Jeff Tang, Jennifer Chan, Jenni Zhen, Jeremy Reizenstein, Jeremy Teboul, Jessica Zhong, Jian Jin, Jingyi Yang, Joe Cummings, Jon Carvill, Jon Shepard, Jonathan McPhie, Jonathan Torres, Josh Ginsburg, Junjie Wang, Kai Wu, Kam Hou U, Karan Saxena, Karthik Prasad, Kartikay Khandelwal, Katayoun

- Zand, Kathy Matosich, Kaushik Veeraraghavan, Kelly Michelena, Keqian Li, Kun Huang, Kunal Chawla, Kushal Lakhotia, Kyle Huang, Lailin Chen, Lakshya Garg, Lavender A, Leandro Silva, Lee Bell, Lei Zhang, Liangpeng Guo, Licheng Yu, Liron Moshkovich, Luca Wehrstedt, Madian Khabza, Manav Avalani, Manish Bhatt, Maria Tsimpoukelli, Marynas Mankus, Matan Hasson, Matthew Lennie, Matthias Reso, Maxim Groshev, Maxim Naumov, Maya Lathi, Meghan Keneally, Michael L. Seltzer, Michal Valko, Michelle Restrepo, Mihir Patel, Mik Vyatskov, Mikayel Samvelyan, Mike Clark, Mike Macey, Mike Wang, Miquel Jubert Hermoso, Mo Metanat, Mohammad Rastegari, Munish Bansal, Nandhini Santhanam, Natascha Parks, Natasha White, Navyata Bawa, Nayan Singhal, Nick Egebo, Nicolas Usunier, Nikolay Pavlovich Laptev, Ning Dong, Ning Zhang, Norman Cheng, Oleg Chernoguz, Olivia Hart, Omkar Salpekar, Ozlem Kalinli, Parkin Kent, Parth Parekh, Paul Saab, Pavan Balaji, Pedro Rittner, Philip Bontrager, Pierre Roux, Piotr Dollár, Polina Zvyagina, Prashant Ratanchandani, Pritish Yuvraj, Qian Liang, Rachad Alao, Rachel Rodriguez, Rafi Ayub, Raghotham Murthy, Raghu Nayani, Rahul Mitra, Raymond Li, Rebekkah Hogan, Robin Battey, Rocky Wang, Rohan Maheswari, Russ Howes, Ruty Rinott, Sai Jayesh Bondu, Samyak Datta, Sara Chugh, Sara Hunt, Sargun Dhillon, Sasha Sidorov, Satadru Pan, Saurabh Verma, Seiji Yamamoto, Sharadh Ramaswamy, Shaun Lindsay, Shaun Lindsay, Sheng Feng, Shenghao Lin, Shengxin Cindy Zha, Shiva Shankar, Shuang Zhang, Shuang Zhang, Sinong Wang, Sneha Agarwal, Soji Sajuyigbe, Soumith Chintala, Stephanie Max, Stephen Chen, Steve Kehoe, Steve Satterfield, Sudarshan Govindaprasad, Sumit Gupta, Sungmin Cho, Sunny Virk, Suraj Subramanian, Sy Choudhury, Sydney Goldman, Tal Remez, Tamar Glaser, Tamara Best, Thilo Kohler, Thomas Robinson, Tianhe Li, Tianjun Zhang, Tim Matthews, Timothy Chou, Tzook Shaked, Varun Vontimitta, Victoria Ajayi, Victoria Montanez, Vijai Mohan, Vinay Satish Kumar, Vishal Mangla, Vitor Albiero, Vlad Ionescu, Vlad Poenaru, Vlad Tiberiu Mihailescu, Vladimir Ivanov, Wei Li, Wenchen Wang, Wenwen Jiang, Wes Bouaziz, Will Constable, Xiaocheng Tang, Xiaofang Wang, Xiaojian Wu, Xiaolan Wang, Xide Xia, Xilun Wu, Xinbo Gao, Yanjun Chen, Ye Hu, Ye Jia, Ye Qi, Yenda Li, Yilin Zhang, Ying Zhang, Yossi Adi, Youngjin Nam, Yu, Wang, Yuchen Hao, Yundi Qian, Yuzi He, Zach Rait, Zachary DeVito, Zef Rosnbrick, Zhaoduo Wen, Zhenyu Yang, and Zhiwei Zhao. 2024. The Llama 3 Herd of Models. arXiv:2407.21783 [cs.AI] <https://arxiv.org/abs/2407.21783>
- [23] D.G. Elliott, M. Stumm, W.M. Snelgrove, C. Cococar, and R. Mckenzie. 1999. Computational RAM: implementing processors in memory. *IEEE Design & Test of Computers* 16, 1 (1999), 32–41. doi:10.1109/54.748803
- [24] Elias Frantar, Saleh Ashkboos, Torsten Hoefer, and Dan Alistarh. 2023. GPTQ: Accurate Post-Training Quantization for Generative Pre-trained Transformers. arXiv:2210.17323 [cs.LG] <https://arxiv.org/abs/2210.17323>
- [25] Hidehiro Fujiwara, Haruki Mori, Wei-Chang Zhao, Kinshuk Khare, Cheng-En Lee, Xiaochen Peng, Vineet Joshi, Chao-Kai Chuang, Shu-Huan Hsu, Takeshi Hashizume, Toshiaki Naganuma, Chen-Hung Tien, Yao-Yi Liu, Yen-Chien Lai, Chia-Fu Lee, Tan-Li Chou, Kerem Akarvardar, Saman Adham, Yih Wang, Yu-Der Chih, Yen-Huei Chen, Hung-Jen Liao, and Tsung-Yung Jonathan Chang. 2024. 34.4 A 3nm, 32.5TOPS/W, 55.0TOPS/mm² and 3.78Mb/mm² Fully-Digital Compute-in-Memory Macro Supporting INT12 × INT12 with a Parallel-MAC Architecture and Foundry 6T-SRAM Bit Cell. In *2024 IEEE International Solid-State Circuits Conference (ISSCC)*, Vol. 67. 572–574. doi:10.1109/ISSCC49657.2024.10454556
- [26] Mingyu Gao, Xuan Yang, Jing Pu, Mark Horowitz, and Christos Kozyrakis. 2019. TANGRAM: Optimized Coarse-Grained Dataflow for Scalable NN Accelerators (ASPLOS '19). Association for Computing Machinery, New York, NY, USA, 807–820. doi:10.1145/3297858.3304014
- [27] Sujan K. Gonugondla, Charbel Sakr, Hassan Dbouk, and Naresh R. Shanbhag. 2022. Fundamental Limits on Energy-Delay-Accuracy of In-Memory Architectures in Inference Applications. *IEEE Transactions on Computer-Aided Design of Integrated Circuits and Systems* 41, 10 (2022), 3188–3201. doi:10.1109/TCAD.2021.3124757
- [28] Graphcore. 2022. *The wow factor*. <https://www.graphcore.ai/posts/the-wow-factor-graphcore-systems-get-huge-power-and-efficiency-boost>
- [29] Graphcore. 2024. *IPU*. <https://www.graphcore.ai/bow-processors>
- [30] An Guo, Xin Si, Xi Chen, Fangyuan Dong, Xingyu Pu, Dongqi Li, Yongliang Zhou, Lizheng Ren, Yeyang Xue, Xueshan Dong, Hui Gao, Yiran Zhang, Jingmin Zhang, Yuyao Kong, Tianzhu Xiong, Bo Wang, Hao Cai, Weiwei Shan, and Jun Yang. 2023. A 28nm 64-kb 31.6-TFLOPS/W Digital-Domain Floating-Point-Computing-Unit and Double-Bit 6T-SRAM Computing-in-Memory Macro for Floating-Point CNNs. In *2023 IEEE International Solid-State Circuits Conference (ISSCC)*. 128–130. doi:10.1109/ISSCC42615.2023.10067260
- [31] Manjari Gupta, Lava Bhargava, and S. Indu. 2021. Dynamic workload-aware DVFS for multicore systems using machine learning. *Computing* 103, 8 (Aug. 2021), 1747–1769. doi:10.1007/s00607-020-00845-2
- [32] Heather Hanson, Stephen W. Keckler, Soraya Ghiasi, Karthick Rajamani, Freeman Rawson, and Juan Rubio. 2007. Thermal response to DVFS: analysis with an Intel Pentium M. In *Proceedings of the 2007 international symposium on Low power electronics and design (ISLPED '07)*. 219–224. doi:10.1145/1283780.1283827
- [33] Kaiming He, Xiangyu Zhang, Shaoqing Ren, and Jian Sun. 2016. Deep Residual Learning for Image Recognition. In *2016 IEEE Conference on Computer Vision and Pattern Recognition (CVPR)*. 770–778. doi:10.1109/CVPR.2016.90
- [34] Yifan He, Haikang Diao, Chen Tang, Wenbin Jia, Xiyuan Tang, Yuan Wang, Jinshan Yue, Xueqing Li, Huazhong Yang, Hongyang Jia, and Yongpan Liu. 2023. 7.3 A 28nm 38-to-102-TOPS/W 8b Multiply-Less Approximate Digital SRAM Compute-In-Memory Macro for Neural-Network Inference. In *2023 IEEE International Solid-State Circuits Conference (ISSCC)*. 130–132. doi:10.1109/ISSCC42615.2023.10067305
- [35] Sun ik Heo, Andrew B. Kahng, Minsoo Kim, Lutong Wang, and Chutong Yang. 2019. Detailed Placement for IR Drop Mitigation by Power Staple Insertion in Sub-10nm VLSI. In *2019 Design, Automation & Test in Europe Conference & Exhibition (DATE)*. 830–835. doi:10.23919/DATE.2019.8715096
- [36] Houmo. 2024. *HaloDrive™30*. <https://www.houmoai.com/en/48/ProductType.html>
- [37] Houmo. 2024. *MoMagic™30*. <https://www.houmoai.com/en/55/ProductType.html>
- [38] Essam H. Houssein, Ahmed G. Gad, Yaser M. Wazery, and Ponnuthurai Nagaratan Suganthan. 2021. Task Scheduling in Cloud Computing based on Metaheuristics: Review, Taxonomy, Open Challenges, and Future Trends. *Swarm and Evolutionary Computation* 62 (April 2021), 100841. doi:10.1016/j.swevo.2021.100841
- [39] Andrew G. Howard, Menglong Zhu, Bo Chen, Dmitry Kalenichenko, Weijun Wang, Tobias Weyand, Marco Andreetto, and Hartwig Adam. 2017. MobileNets: Efficient Convolutional Neural Networks for Mobile Vision Applications. arXiv:1704.04861 [cs.CV]
- [40] Jason Howard, Saurabh Dighe, Yatin Hoskote, Sriram Vangal, David Finan, Gregory Ruhl, David Jenkins, Howard Wilson, Nitin Borkar, Gerhard Schrom, Fabrice Paillet, Shailendra Jain, Tiju Jacob, Satish Yada, Sraven Marella, Praveen Salihundam, Vasantha Erraguntla, Michael Konow, Michael Riepen, Guido Droege, Joerg Lindemann, Matthias Gries, Thomas Apel, Kersten Henriss, Tor Lund-Larsen, Sebastian Steibl, Shekhar Borkar, Vivek De, Rob Van Der Wijngaart, and Timothy Mattson. 2010. A 48-Core IA-32 message-passing processor with DVFS in 45nm CMOS. In *2010 IEEE International Solid-State Circuits Conference - (ISSCC)*. 108–109. doi:10.1109/ISSCC.2010.5434077
- [41] Yihan Hu, Jiazhi Yang, Li Chen, Keyu Li, Chonghao Sima, Xizhou Zhu, Siqi Chai, Senyao Du, Tianwei Lin, Wenhai Wang, Lewei Lu, Xiaosong Jia, Qiang Liu, Jifeng Dai, Yu Qiao, and Hongyang Li. 2023. Planning-oriented Autonomous Driving. In *2023 IEEE/CVF Conference on Computer Vision and Pattern Recognition (CVPR)*. 17853–17862. doi:10.1109/CVPR52729.2023.01712
- [42] Xuan-Xue Huang, Hsien-Chia Chen, Sheng-Wei Wang, Iris Hui-Ru Jiang, Yih-Chih Chou, and Cheng-Hong Tsai. 2020. Dynamic IR-Drop ECO Optimization by Cell Movement with Current Waveform Staggering and Machine Learning Guidance. In *2020 IEEE/ACM International Conference On Computer Aided Design (ICCAD)*. 1–9.
- [43] Daijoon Hyun, Younggwang Jung, Insu Cho, and Youngsoo Shin. 2023. Decoupling Capacitor Insertion Minimizing IR-Drop Violations and Routing DRVs. In *2023 28th Asia and South Pacific Design Automation Conference (ASP-DAC)*. 271–276.
- [44] Xun Jiang, zhuomin chai, Yuxiang Zhao, Yibo Lin, Runsheng Wang, and Ru Huang. 2024. CircuitNet 2.0: An Advanced Dataset for Promoting Machine Learning Innovations in Realistic Chip Design Environment. In *The Twelfth International Conference on Learning Representations*. <https://openreview.net/forum?id=nMF5UjxMlI>
- [45] Vijay Kiran Kalyanam, Eric Mahurin, Keith Bowman, and Jacob Abraham. 2020. A Proactive Voltage-Droop-Mitigation System in a 7nm Hexagon™ Processor. In *2020 IEEE Symposium on VLSI Circuits*. 1–2. doi:10.1109/VLSICircuits18222.2020.9162808
- [46] Asif Ali Khan, João Paulo C. De Lima, Hamid Farzaneh, and Jeronimo Castrillon. 2024. The Landscape of Compute-near-memory and Compute-in-memory: A Research and Commercial Overview. arXiv:2401.14428 [cs.AR] <https://arxiv.org/abs/2401.14428>
- [47] Joonhyung Kim and Jongsun Park. 2022. The Quantitative Comparisons of Analog and Digital SRAM Compute-In-Memories for Deep Neural Network Applications. In *2022 19th International SOC Design Conference (ISOC)*. 129–130. doi:10.1109/ISOC56007.2022.10031424
- [48] Adrian Kneip and David Bol. 2021. Impact of Analog Non-Idealities on the Design Space of 6T-SRAM Current-Domain Dot-Product Operators for In-Memory Computing. *IEEE Transactions on Circuits and Systems I: Regular Papers* 68, 5 (2021), 1931–1944. doi:10.1109/TCSI.2021.3058510
- [49] Adrian Kneip, Martin Lefebvre, Julien Verecken, and David Bol. 2023. IMPACT: A 1-to-4b 813-TOPS/W 22-nm FD-SOI Compute-in-Memory CNN Accelerator Featuring a 4.2-POPS/W 146-TOPS/mm² CIM-SRAM With Multi-Bit Analog Batch-Normalization. *IEEE Journal of Solid-State Circuits* 58, 7 (2023), 1871–1884. doi:10.1109/JSSC.2023.3269098
- [50] Eldar Kurtic and Dan Alistarh. 2022. GMP*: Well-Tuned Gradual Magnitude Pruning Can Outperform Most BERT-Pruning Methods. arXiv:2210.06384 [cs.CL] <https://arxiv.org/abs/2210.06384>
- [51] Dohyeon Lee, Heecheol Hwang, Hyunteck Oh, and Yongchan James Ban. 2021. Mitigating IR-Drop with Design Technology Co-Optimization for Sub-Nanometer

- Node Technology. In *2021 18th International SoC Design Conference (ISOCC)*. 1–2. doi:10.1109/ISOCC53507.2021.9614021
- [52] Yuhang Li, Ruihao Gong, Xu Tan, Yang Yang, Peng Hu, Qi Zhang, Fengwei Yu, Wei Wang, and Shi Gu. 2021. {BRECQ}: Pushing the Limit of Post-Training Quantization by Block Reconstruction. In *International Conference on Learning Representations*. <https://openreview.net/forum?id=POVv6hDd9XH>
- [53] Jai-Ming Lin, Yang-Tai Kung, Zheng-Yu Huang, and I-Ru Chen. 2021. A Fast Power Network Optimization Algorithm for Improving Dynamic IR-Drop. In *Proceedings of the 2021 International Symposium on Physical Design (Virtual Event, USA) (ISPD '21)*. Association for Computing Machinery, New York, NY, USA, 91–98. doi:10.1145/3439706.3447042
- [54] Tsung-Yi Lin, Michael Maire, Serge Belongie, Lubomir Bourdev, Ross Girshick, James Hays, Pietro Perona, Deva Ramanan, C. Lawrence Zitnick, and Piotr Dollár. 2015. Microsoft COCO: Common Objects in Context. arXiv:1405.0312 [cs.CV] <https://arxiv.org/abs/1405.0312>
- [55] Liangkai Liu, Sidi Lu, Ren Zhong, Baofu Wu, Yongtao Yao, Qingyang Zhang, and Weisong Shi. 2021. Computing Systems for Autonomous Driving: State of the Art and Challenges. *IEEE Internet of Things Journal* 8, 8 (2021), 6469–6486. doi:10.1109/JIOT.2020.3043716
- [56] Qiang Liu and Peiran Zhang. 2024. Methodology for IR Drop Analysis of On-Chip Power Distribution Network under Electromagnetic Pulse Attack. *Journal of Computer-Aided Design & Computer Graphics* 36, 4 (2024), 582–590.
- [57] Zechun Liu, Barlas Oguz, Changsheng Zhao, Ernie Chang, Pierre Stock, Yashar Mehdad, Yangyang Shi, Raghuraman Krishnamoorthi, and Vikas Chandra. 2024. LLM-QAT: Data-Free Quantization Aware Training for Large Language Models. In *Findings of the Association for Computational Linguistics, ACL 2024, Bangkok, Thailand and virtual meeting, August 11–16, 2024*, Lun-Wei Ku, Andre Martins, and Vivek Srikumar (Eds.). Association for Computational Linguistics, 467–484. doi:10.18653/v1/2024.FINDINGS-ACL.26
- [58] Lianbo Ma, Yuee Zhou, Jianlun Ma, Guo Yu, and Qing Li. 2024. One-step forward and backtrack: overcoming zig-zagging in loss-aware quantization training. In *Proceedings of the Thirty-Eighth AAAI Conference on Artificial Intelligence and Thirty-Sixth Conference on Innovative Applications of Artificial Intelligence and Fourteenth Symposium on Educational Advances in Artificial Intelligence (AAAI'24/AAAI'24/EAAI'24)*. AAAI Press, Article 1588, 9 pages. doi:10.1609/aaai.v38i13.29336
- [59] Luca Mattii, Drago Mir Milojevic, Peter Debacker, Yasser Sherazi, Mladen Berekovic, and Praveen Raghavan. 2017. IR-drop aware Design & technology co-optimization for N5 node with different device and cell height options. In *2017 IEEE/ACM International Conference on Computer-Aided Design (ICCAD)*. 89–94. doi:10.1109/ICCAD.2017.8203764
- [60] Stephen Merity, Caiming Xiong, James Bradbury, and Richard Socher. 2016. Pointer Sentinel Mixture Models. arXiv:1609.07843 [cs.CL] <https://arxiv.org/abs/1609.07843>
- [61] Haruki Mori, Wei-Chang Zhao, Cheng-En Lee, Chia-Fu Lee, Yu-Hao Hsu, Chao-Kai Chuang, Takeshi Hashizume, Hao-Chun Tung, Yao-Yi Liu, Shin-Rung Wu, Kerem Akarvardar, Tan-Li Chou, Hidehiro Fujiwara, Yih Wang, Yu-Der Chih, Yen-Huei Chen, Hung-Jen Liao, and Tsung-Yung Jonathan Chang. 2023. A 4nm 6163-TOPS/W/b 4790 – TOPS/mm²/b SRAM Based Digital-Computing-in-Memory Macro Supporting Bit-Width Flexibility and Simultaneous MAC and Weight Update. In *2023 IEEE International Solid-State Circuits Conference (ISSCC)*. 132–134. doi:10.1109/ISSCC42615.2023.10067555
- [62] Onur Mutlu, Saugata Ghose, Juan Gómez-Luna, and Rachata Ausavarungnirun. 2022. A Modern Primer on Processing in Memory. arXiv:2012.03112 [cs.AR]
- [63] Markus Nagel, Rana Ali Amjad, Mart Van Baalen, Christos Louizos, and Tijmen Blankevoort. 2020. Up or down? adaptive rounding for post-training quantization. In *International Conference on Machine Learning*. PMLR, 7197–7206.
- [64] Markus Nagel, Marios Fournarakis, Rana Ali Amjad, Yelysei Bondarenko, Mart Van Baalen, and Tijmen Blankevoort. 2021. A white paper on neural network quantization. arXiv preprint arXiv:2106.08295 (2021).
- [65] S K Nithin, Gowry sankar Shanmugam, and Sreeram Chandrasekar. 2010. Dynamic voltage (IR) drop analysis and design closure: Issues and challenges. In *2010 11th International Symposium on Quality Electronic Design (ISQED)*. 611–617. doi:10.1109/ISQED.2010.5450515
- [66] S K Nithin, Gowry sankar Shanmugam, and Sreeram Chandrasekar. 2010. Dynamic voltage (IR) drop analysis and design closure: Issues and challenges. In *2010 11th International Symposium on Quality Electronic Design (ISQED)*. 611–617. doi:10.1109/ISQED.2010.5450515
- [67] W Oelfner, F Berthold, and U Guth. 2006. The iR drop—well-known but often underestimated in electrochemical polarization measurements and corrosion testing. *Materials and Corrosion* 57, 6 (2006), 455–466.
- [68] Heikki Orsila. 2011. *Optimizing Algorithms for Task Graph Mapping on Multiprocessor System on Chip*. Tampere University of Technology. Awarding institution:Tampere University of Technology-
Submitter:Submitted by Heikki Orsila (heikki.orsila@tut.fi) on 2011-05-11T20:37:07Z No. of bitstreams: 1 thesis-without-cover-2011-05-10.pdf: 6018965 bytes, checksum: 2fde471ec8ab26a7008a209bcd893e8c (MD5)-
Submitter:Approved for entry into archive by Kaisa Kulkki(kaisa.kulkki@tut.fi) on 2011-05-13T11:43:58Z (GMT) No. of bitstreams: 1 thesis-without-cover-2011-05-10.pdf: 6018965 bytes, checksum: 2fde471ec8ab26a7008a209bcd893e8c (MD5)-
Submitter:Made available in DSpace on 2011-05-13T11:43:58Z (GMT). No. of bitstreams: 1 thesis-without-cover-2011-05-10.pdf: 6018965 bytes, checksum: 2fde471ec8ab26a7008a209bcd893e8c (MD5).
- [69] PIMCHIP. 2024. S200. <https://www.pimchip.cn/article/67.html>
- [70] Alec Radford, Jeffrey Wu, Rewon Child, David Luan, Dario Amodei, Ilya Sutskever, et al. 2019. Language models are unsupervised multitask learners. *OpenAI blog* 1, 8 (2019), 9.
- [71] Erxiang Ren, Jiahui Liu, Li Luo, Xinghua Yang, Qi Wei, and Fei Qiao. 2024. NS-Engine: Near-Sensor Neural Network Engine with SRAM-Based Compute-in-Memory Macro. In *2024 IEEE International Symposium on Circuits and Systems (ISCAS)*. 1–5. doi:10.1109/ISCAS58744.2024.10557977
- [72] Olga Russakovsky, Jia Deng, Hao Su, Jonathan Krause, Sanjeev Satheesh, Sean Ma, Zhiheng Huang, Andrej Karpathy, Aditya Khosla, Michael Bernstein, et al. 2015. Imagenet large scale visual recognition challenge. *International journal of computer vision* 115 (2015), 211–252.
- [73] Jayashree Saxena, Kenneth M Butler, Vinay B Jayaram, Subhendu Kundu, NV Arvind, Pravin Sreepakash, and Manfred Hachinger. 2003. A case study of IR-drop in structured at-speed testing. In *International Test Conference, 2003. Proceedings. ITC 2003*. IEEE Computer Society, 1098–1098.
- [74] Weiwei Shan, Kaize Zhou, Keran Li, Yuxuan Du, Zhuo Chen, Junyi Qian, Haitao Ge, Jun Yang, and Xin Si. 2024. 14.2 Proactive Voltage Droop Mitigation Using Dual-Proportional-Derivative Control Based on Current and Voltage Prediction Applied to a Multicore Processor in 28nm CMOS. In *IEEE International Solid-State Circuits Conference, ISSCC 2024, San Francisco, CA, USA, February 18–22, 2024*. IEEE, 256–258. doi:10.1109/ISSCC49657.2024.10454398
- [75] Wenqi Shao, Mengzhao Chen, Zhaoyang Zhang, Peng Xu, Lirui Zhao, Zhiqian Li, Kaipeng Zhang, Peng Gao, Yu Qiao, and Ping Luo. 2024. OmniQuant: Omni-directionally Calibrated Quantization for Large Language Models. In *The Twelfth International Conference on Learning Representations*. <https://openreview.net/forum?id=8Wuvvh0LYW>
- [76] K.L. Shepard and V. Narayanan. 1996. Noise in deep submicron digital design. In *Proceedings of International Conference on Computer Aided Design*. 524–531. doi:10.1109/ICCAD.1996.569906
- [77] Shinichi Shibahara, Chikafumi Takahashi, Kazuki Fukuoka, Yuko Kitaji, Takahiro Irita, Hirokata Hara, Yasuhisa Shimazaki, and Jun Matsushima. 2017. A 16 nm FinFET Heterogeneous Nona-Core SoC Supporting ISO26262 ASIL B Standard. *IEEE Journal of Solid-State Circuits* 52, 1 (2017), 77–88. doi:10.1109/JSSC.2016.2623682
- [78] Ming-En Shih, Shih-Wei Hsieh, Ping-Yuan Tsai, Ming-Hung Lin, Pei-Kuei Tsung, En-Jui Chang, Jenwei Liang, Shu-Hsin Chang, Chung-Lun Huang, You-Yu Nian, Zhe Wan, Sushil Kumar, Cheng-Xin Xue, Gajanan Jedhe, Hidehiro Fujiwara, Haruki Mori, Chih-Wei Chen, Po-Hua Huang, Chih-Feng Juan, Chung-Yi Chen, Tsung-Yao Lin, Ch Wang, Chih-Cheng Chen, and Kevin Jou. 2024. 20.1 NVE: A 3nm 23.2TOPS/W 12b-Digital-CIM-Based Neural Engine for High-Resolution Visual-Quality Enhancement on Smart Devices. In *2024 IEEE International Solid-State Circuits Conference (ISSCC)*, Vol. 67. 360–362. doi:10.1109/ISSCC49657.2024.10454482
- [79] Xin Si, Yung-Ning Tu, Wei-Hsing Huang, Jian-Wei Su, Pei-Jung Lu, Jing-Hong Wang, Ta-Wei Liu, Ssu-Yen Wu, Ruhui Liu, Yen-Chi Chou, Yen-Lin Chung, William Shih, Chung-Chuan Lo, Ren-Shuo Liu, Chih-Cheng Hsieh, Kea-Tiong Tang, Nan-Chun Lien, Wei-Chiang Shih, Yajuan He, Qiang Li, and Meng-Fan Chang. 2021. A Local Computing Cell and 6T SRAM-Based Computing-in-Memory Macro With 8-b MAC Operation for Edge AI Chips. *IEEE Journal of Solid-State Circuits* 56, 9 (2021), 2817–2831. doi:10.1109/JSSC.2021.3073254
- [80] Xin Si, Yung-Ning Tu, Wei-Hsing Huang, Jian-Wei Su, Pei-Jung Lu, Jing-Hong Wang, Ta-Wei Liu, Ssu-Yen Wu, Ruhui Liu, Yen-Chi Chou, Zhixiao Zhang, Suyuan-Hao Sie, Wei-Chen Wei, Yun-Chen Lo, Tai-Hsing Wen, Tzu-Hsiang Hsu, Yen-Kai Chen, William Shih, Chung-Chuan Lo, Ren-Shuo Liu, Chih-Cheng Hsieh, Kea-Tiong Tang, Nan-Chun Lien, Wei-Chiang Shih, Yajuan He, Qiang Li, and Meng-Fan Chang. 2020. 15.5 A 28nm 64Kb 6T SRAM Computing-in-Memory Macro with 8b MAC Operation for AI Edge Chips. In *2020 IEEE International Solid-State Circuits Conference - (ISSCC)*. 246–248. doi:10.1109/ISSCC19947.2020.9062995
- [81] Surecore. 2024. *compuRAM*. <https://www.sure-core.com/products-and-services/#compuram-product>
- [82] synopsys. 2024. *HSPICE*. <https://www.synopsys.com/>
- [83] Synthara. 2024. *ComputeRAM*. <https://synthara.ai/product/>
- [84] Mohammad Tehranipoor and Kenneth M. Butler. 2010. Power Supply Noise: A Survey on Effects and Research. *IEEE Design & Test of Computers* 27, 2 (2010), 51–67. doi:10.1109/MDT.2010.52
- [85] Tsu-Wei Tseng, Chang-Tzu Lin, Chia-Hsin Lee, Yung-Fa Chou, and Ding-Ming Kwai. 2014. A power delivery network (PDN) engineering change order (ECO) approach for repairing IR-drop failures after the routing stage. In *Technical Papers of 2014 International Symposium on VLSI Design, Automation and Test*. 1–4. doi:10.1109/VLSI-DAT.2014.6834874

- [86] Fengbin Tu, Yiqi Wang, Zihan Wu, Weiwei Wu, Leibo Liu, Yang Hu, Shaojun Wei, and Shouyi Yin. 2023. 16.4 TensorCIM: A 28nm 3.7nJ/Gather and 8.3TFLOPS/W FP32 Digital-CIM Tensor Processor for MCM-CIM-Based Beyond-NN Acceleration. In *2023 IEEE International Solid-State Circuits Conference (ISSCC)*. 254–256. doi:10.1109/ISSCC42615.2023.10067285
- [87] Fengbin Tu, Zihan Wu, Yiqi Wang, Weiwei Wu, Leibo Liu, Yang Hu, Shaojun Wei, and Shouyi Yin. 2023. 16.1 MulTCIM: A 28nm 2.24 μ J/Token Attention-Token-Bit Hybrid Sparse Digital CIM-Based Accelerator for Multimodal Transformers. In *2023 IEEE International Solid-State Circuits Conference (ISSCC)*. 248–250. doi:10.1109/ISSCC42615.2023.10067842
- [88] Peter JM Van Laarhoven, Emile HL Aarts, Peter JM van Laarhoven, and Emile HL Aarts. 1987. *Simulated annealing*. Springer.
- [89] Yipeng Wang, Mengtian Yang, Chieh-Pu Lo, and Jaydeep P. Kulkarni. 2024. 30.6 Vecim: A 289.13GOPS/W RISC-V Vector Co-Processor with Compute-in-Memory Vector Register File for Efficient High-Performance Computing. In *2024 IEEE International Solid-State Circuits Conference (ISSCC)*, Vol. 67. 492–494. doi:10.1109/ISSCC49657.2024.10454387
- [90] Ping-Chun Wu, Jian-Wei Su, Li-Yang Hong, Jin-Sheng Ren, Chih-Han Chien, Ho-Yu Chen, Chao-En Ke, Hsu-Ming Hsiao, Sih-Han Li, Shyh-Shyuan Sheu, Wei-Chung Lo, Shih-Chieh Chang, Chung-Chuan Lo, Ren-Shuo Liu, Chih-Cheng Hsieh, Kea-Tiong Tang, and Meng-Fan Chang. 2023. A 22nm 832Kb Hybrid-Domain Floating-Point SRAM In-Memory-Compute Macro with 16.2-70.2TFLOPS/W for High-Accuracy AI-Edge Devices. In *2023 IEEE International Solid-State Circuits Conference (ISSCC)*. 126–128. doi:10.1109/ISSCC42615.2023.10067527
- [91] Bonan Yan, Jeng-Long Hsu, Pang-Cheng Yu, Chia-Chi Lee, Yaojun Zhang, Wenshuo Yue, Guoqiang Mei, Yuchao Yang, Yue Yang, Hai Li, Yiran Chen, and Ru Huang. 2022. A 1.041-Mb/mm² 27.38-TOPS/W Signed-INT8 Dynamic-Logic-Based ADC-less SRAM Compute-in-Memory Macro in 28nm with Reconfigurable Bitwise Operation for AI and Embedded Applications. In *2022 IEEE International Solid-State Circuits Conference (ISSCC)*, Vol. 65. 188–190. doi:10.1109/ISSCC42614.2022.9731545
- [92] Chenyu Yang, Yuntao Chen, Hao Tian, Chenxin Tao, Xizhou Zhu, Zhaoxiang Zhang, Gao Huang, Hongyang Li, Yu Qiao, Lewei Lu, Jie Zhou, and Jifeng Dai. 2023. BEVFormer v2: Adapting Modern Image Backbones to Bird's-Eye-View Recognition via Perspective Supervision. In *2023 IEEE/CVF Conference on Computer Vision and Pattern Recognition (CVPR)*. 17830–17839. doi:10.1109/CVPR52729.2023.01710
- [93] Kentaro Yoshioka, Shimpei Ando, Satomi Miyagi, Yung-Chin Chen, and Wen-lun Zhang. 2024. A Review of SRAM-based Compute-in-Memory Circuits. arXiv:2411.06079 [cs.AR] <https://arxiv.org/abs/2411.06079>
- [94] Shimeng Yu, Hongwu Jiang, Shanshi Huang, Xiaochen Peng, and Anni Lu. 2021. Compute-in-Memory Chips for Deep Learning: Recent Trends and Prospects. *IEEE Circuits and Systems Magazine* 21, 3 (2021), 31–56. doi:10.1109/MCAS.2021.3092533
- [95] Jinshan Yue, Chaojie He, Zi Wang, Zhaori Cong, Yifan He, Mufeng Zhou, Wenyu Sun, Xueqing Li, Chunmeng Dou, Feng Zhang, Huazhong Yang, Yongpan Liu, and Ming Liu. 2023. A 28nm 16.9-300TOPS/W Computing-in-Memory Processor Supporting Floating-Point NN Inference/Training with Intensive-CIM Sparse-Digital Architecture. In *2023 IEEE International Solid-State Circuits Conference (ISSCC)*. 1–3. doi:10.1109/ISSCC42615.2023.10067779
- [96] Ekim Yurtsever, Jacob Lambert, Alexander Carballo, and Kazuya Takeda. 2020. A Survey of Autonomous Driving: Common Practices and Emerging Technologies. *IEEE Access* 8 (2020), 58443–58469. doi:10.1109/ACCESS.2020.2983149
- [97] Dongping Zhang, Nuwan Jayasena, Alexander Lyashevsky, Joseph L. Greathouse, Lifan Xu, and Michael Ignatowski. 2014. TOP-PIM: throughput-oriented programmable processing in memory. In *Proceedings of the 23rd International Symposium on High-Performance Parallel and Distributed Computing (Vancouver, BC, Canada) (HPDC '14)*. Association for Computing Machinery, New York, NY, USA, 85–98. doi:10.1145/2600212.2600213
- [98] Yundong Zhang, Huiye Liu, and Qiang Hu. 2021. TransFuse: Fusing Transformers and CNNs for Medical Image Segmentation. arXiv:2102.08005 [cs.CV] <https://arxiv.org/abs/2102.08005>
- [99] Size Zheng, Siyuan Chen, and Yun Liang. 2023. Memory and Computation Coordinated Mapping of DNNs onto Complex Heterogeneous SoC. In *2023 60th ACM/IEEE Design Automation Conference (DAC)*. 1–6. doi:10.1109/DAC56929.2023.10247951